

# Transcriptomic Changes toward Osteogenic Differentiation of Mesenchymal Stem Cells on 3D-Printed GelMA/CNC Hydrogel under Pulsatile Pressure Environment

Keya Ganguly, Sayan Deb Dutta, Aayushi Randhawa, Dinesh K. Patel, Tejal V. Patil, and Ki-Taek Lim\*

**Biomimetic soft hydrogels used in bone tissue engineering frequently produce unsatisfactory outcomes. Here, it is investigated how human bone-marrow-derived mesenchymal stem cells (hBMSCs) differentiated into early osteoblasts on remarkably soft 3D hydrogel ( $70 \pm 0.00049$  Pa). Specifically, hBMSCs seeded onto cellulose nanocrystals incorporated methacrylate gelatin hydrogels are subjected to pulsatile pressure stimulation (PPS) of 5–20 kPa for 7 days. The PPS stimulates cellular processes such as mechanotransduction, cytoskeletal distribution, prohibition of oxidative stress, calcium homeostasis, osteogenic marker gene expression, and osteo-specific cytokine secretions in hBMSCs on soft substrates. The involvement of Piezo 1 is the main ion channel involved in mechanotransduction. Additionally, RNA-sequencing results reveal differential gene expression concerning osteogenic differentiation, bone mineralization, ion channel activity, and focal adhesion. These findings suggest a practical and highly scalable method for promoting stem cell commitment to osteogenesis on soft matrices for clinical reconstruction.**

combined action of stiff scaffolds ( $\approx 30$ – $40$  kPa), stem cells, and bioactive molecules.<sup>[2]</sup> Despite these efforts, the formation of new bones still takes several weeks, depending on the size and complexity of bone injury.<sup>[3]</sup> One of the current challenges in BTE is achieving soft hydrogel-based bone regenerative medicine strategies since it is injectable and economical. However, soft hydrogels often fail to provide sufficient mechanical and mechanotransduction-based stimuli necessary for osteogenic differentiation,<sup>[4]</sup> even though physiological bone development through the intramembranous ossification occurs by the direct differentiation of mesenchymal stem cells (MSCs) within a soft physiological matrix ( $\approx 100$ – $1000$  Pa).<sup>[5]</sup>

In this regard, a few notable developments have been made in controlling the osteogenic differentiation of human bone-marrow-derived mesenchymal stem

cells (hBMSCs) on soft hydrogels, such as soft hydrogels mimic intact bone marrow mechanics.<sup>[6]</sup> Wei et al. reported the fabrication of degradable, soft hydrogels ( $\approx 0.5$  kPa) to enhance the proliferation and osteogenic differentiation of C2C12 myoblasts under bone morphogenetic protein 2 (BMP-2) supplementation.<sup>[7]</sup> The osteogenic differentiation of MSCs has been achieved on soft hydrogel of hyaluronic acid with an elastic modulus of  $\approx 2600 \pm 30$  Pa upon BMP-2 incorporation. Bone marrow mimicking hydrogel of polyethylene glycol has been developed by Jansen et al., with a modulus of  $\approx 4.4 \pm 1.0$  kPa that promoted osteogenesis upon the incorporation of bone-marrow-specific peptides.<sup>[8]</sup> Besides, soft hydrogels ( $\approx 3$  kPa) with surface patterning-based nanoarray have been shown to promote osteogenic differentiation of hBMSCs by activating focal adhesion and ion channel expression.<sup>[9]</sup> Biomimetic gelatin methacrylate (GelMA) hydrogel with a modulus of 14.22 kPa has also been shown to promote osteogenic differentiation of BMSCs through enhanced cell-to-surface interaction.<sup>[10]</sup> All these soft hydrogels could achieve noticeable osteogenic differentiation of hBMSCs by enhancing better cell–matrix adhesion. However, incorporating chemical or biomolecular entities often pose challenges regarding scalability and cost-effectiveness. Hence, a cost-effective method to achieve osteogenic commitment of stem cells on soft hydrogels is necessary.

## 1. Introduction

Orthopedic injuries, such as fractures, account for over two million cases annually.<sup>[1]</sup> Bone tissue engineering (BTE) has been widely studied to regenerate new functional bones via the

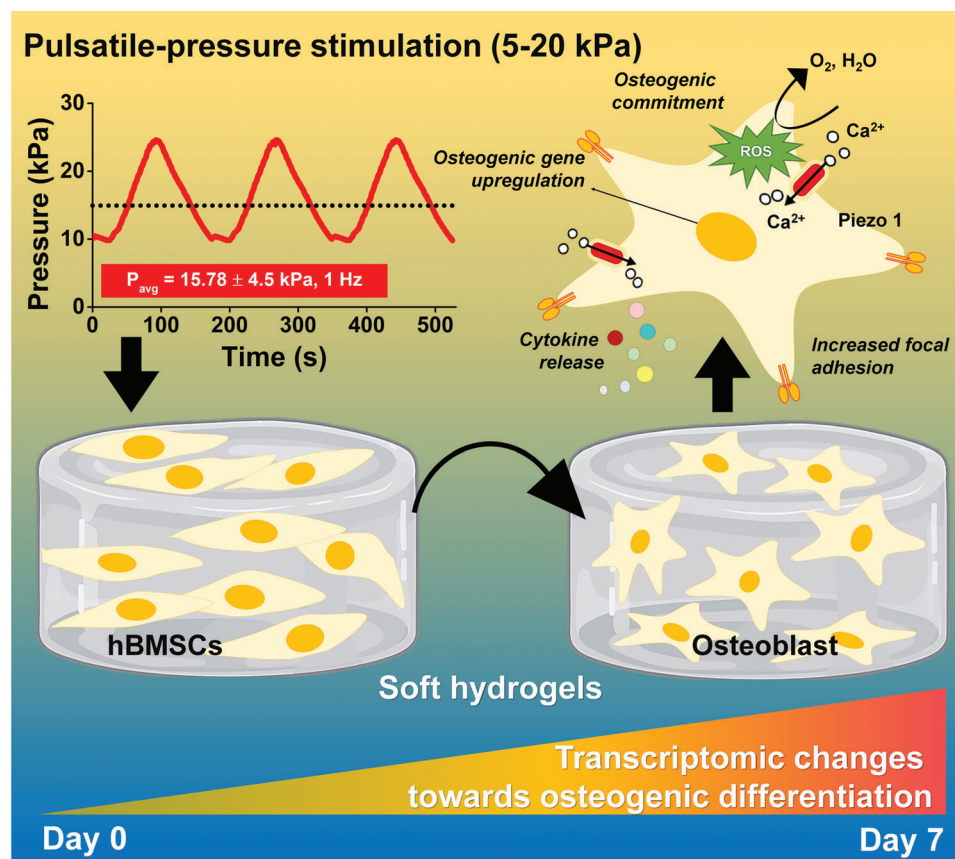
K. Ganguly, S. D. Dutta, A. Randhawa, T. V. Patil, K.-T. Lim  
Department of Biosystems Engineering  
Kangwon National University  
Chuncheon 24341, Republic of Korea  
E-mail: ktlim@kangwon.ac.kr

A. Randhawa, T. V. Patil, K.-T. Lim  
Interdisciplinary Program in Smart Agriculture  
Kangwon National University  
Chuncheon 24341, Republic of Korea  
D. K. Patel, K.-T. Lim  
Institute of Forest Science  
Kangwon National University  
Chuncheon 24341, Republic of Korea

K.-T. Lim  
Biomechagen Co., Ltd.  
Chuncheon 24341, Republic of Korea

 The ORCID identification number(s) for the author(s) of this article can be found under <https://doi.org/10.1002/adhm.202202163>

DOI: 10.1002/adhm.202202163



**Scheme 1.** Schematic illustration of the effect of pulsatile pressure stimulation on the osteogenic commitment of human mesenchymal stem cells (hBMSCs) cultured on soft hydrogel matrix.

Several pressure bioreactors have been designed to promote osteogenic differentiation to develop bone grafts.<sup>[11]</sup> Pulsatile mechanical stimulations are beneficial for bone regeneration as bone is mechanosensitive tissue that constantly experiences pulsatile mechanical stress in the normal physiological condition.<sup>[12]</sup> Moreover, pressure stimulation as low as 10 kPa has been found to drive hBMSCs osteogenic lineage commitment.<sup>[13]</sup> However, whether mechanical stimulation can trigger osteogenic differentiation on super soft matrices remains veiled. Also, the molecular mechanisms concerning mechanotransduction on soft substrates are vague.

In this work, we developed a custom-designed bioreactor for the pulsatile pressure stimulation (PPS) of 5–20 kPa on hBMSCs in a very soft hydrogel ( $70 \pm 0.00049$  Pa) microenvironment. We used cellulose nanocrystals (CNCs) incorporated GelMA hydrogels (GelMA) as a platform for hBMSCs mechanical stimulation. CNC is often used as a nanofiller for GelMA-based bioinks to improve their mechanical properties. We proposed that a PPS range of 5–20 kPa could manipulate hBMSCs mechanotransduction for osteogenic differentiation on soft GelMA hydrogel (Scheme 1). The cell–matrix interactions were characterized at the cellular and functional levels, including biocompatibility assessment, stress-induced oxidative damage, mineralization, cell adhesion, cytoskeletal orientation, gene and protein expression, cytokine, and chemokine release related to hBMSCs osteogenic differentiation. We further correlated our data with transcrip-

tom changes through RNA-sequencing analysis. Our data suggest that soft and flexible hydrogels with modulus as low as  $70 \pm 0.00049$  Pa can promote osteogenic differentiation under 5–20 kPa PPS. We anticipate that our findings advance the existing insight on mechanotransduction-induced osteogenic differentiation. Also, the PPS can be adopted in bone regeneration under clinical setups involving soft hydrogel-based BTE and can foster the fabrication of innovative, cost-effective, and scalable bone grafts.

## 2. Results

### 2.1. Physicochemical Characterization of Hydrogels

Protein-based hydrogels, such as Matrigel, are commercially used as extracellular matrix analogs for tissue engineering applications because of their excellent biocompatibility and bioactive properties.<sup>[14]</sup> GelMA is a potential alternative to Matrigel for bio-applications, including osteogenic differentiation.<sup>[15]</sup> GelMA is synthesized using gelatin with methacrylic anhydride (MAA), and the degree of methacrylation (DM) can be adjusted to influence the bio-physicochemical properties of the construct, including mechanical properties, biocompatibility, and cell adhesion. Moreover, GelMA is an excellent candidate for 3D printing.<sup>[16]</sup> Hence, we chose GelMA for the fabrication of the 3D-printed construct. We synthesized photocrosslinkable GelMA by

functionalizing the primary amine groups of gelatin with MAA, and the success of the synthesis along with the DM was determined using NMR spectroscopy. The  $^1\text{H}$  NMR spectra of pure gelatin and GelMA are shown in Figure S1 in the Supporting Information. The characteristic peak for gelatin was observed in both the samples; the proton peak observed at 7.1–7.4 ppm indicated the presence of phenylalanine and the peak at 2.8–3.0 ppm appeared owing to lysine methylene.<sup>[17]</sup> Additionally, the new peaks at 5.4 and 5.6 ppm indicated the successful binding of the methacrylate groups to gelatin. The DM of GelMA was calculated to be  $\approx 25\%$ ,  $\approx 50\%$ , and  $71.44 \pm 0.32\%$  as determined by the ratio of the integrated area of the lysine methylene signals (2.8–3.0 ppm) of GelMA and the phenylalanine signal (7.1–7.4 ppm) of unmodified gelatin.<sup>[18]</sup> The DM obtained in our study for GelMA agreed with the previously reported values in the literature with excellent biocompatibility.<sup>[15a,16b,17b,19]</sup> As our study aimed to evaluate the effect of mechanical stimulation on hBMSCs differentiation, we next incorporated CNCs to develop a mechanically more stable GelMA-CNC (CelMA) hydrogel.<sup>[20]</sup>

We performed attenuated total reflection-Fourier transform infrared (ATR-FTIR) analysis to characterize the chemical compositions of fabricated GelMA and CelMA hydrogels (Figure S2, Supporting Information). Characteristic peaks were observed in the FTIR spectrum of GelMA at  $\approx 3292\text{ cm}^{-1}$ , indicating the N–H stretch of amide (II) and at  $\approx 2936\text{ cm}^{-1}$  corresponding to the C–H stretch. Moreover, the peaks at  $\approx 1631$ ,  $1531$ , and  $1235\text{ cm}^{-1}$  confirmed the C=O stretching vibration of the amide groups, N–H bending vibration of amide (II), and N–H bending of amide (III), respectively. The FTIR spectra of the prepared CNCs showed peaks at  $3330\text{ cm}^{-1}$  (–OH region),  $2898\text{ cm}^{-1}$  (C–H stretching vibration),  $1427\text{ cm}^{-1}$  (symmetric bending), and  $1314\text{ cm}^{-1}$  ( $\text{CH}_2$  wagging at C6). The peaks at  $1160$ ,  $1104$ , and  $1053\text{ cm}^{-1}$  corresponded to the sulfate ester bonds formed due to sulfuric acid hydrolysis during CNC preparation. The peaks appeared at  $\approx 3319$ ,  $2122$ , and  $1636\text{ cm}^{-1}$  for the CelMA hydrogel, indicating the presence of OH stretching of carboxylic acid, weak  $\text{C}\equiv\text{C}/\text{N}=\text{C}=\text{N}$  stretching of carbodimide/intense  $\text{N}=\text{N}=\text{N}$  stretching of azide, and  $\text{C}=\text{C}$  stretching, respectively. The appearance of the peaks indicated chemical interactions between GelMA and CNC.

The viscoelastic property of the hydrogel greatly determines the printing behavior and subsequent physicochemical properties under PPS in culture conditions. Hence, estimation of the viscoelastic nature is crucial. The viscoelastic properties of the crosslinked hydrogels were determined using a rotational rheometer in the angular frequency ( $\omega$ ) range of 0.1 to  $100\text{ rad s}^{-1}$  at room temperature (RT). The changes in the storage modulus ( $G'$ ) and loss modulus ( $G''$ ) of the hydrogels, along with the changes in their viscosities in the measured  $\omega$  ranges, are shown in Figure S3 in the Supporting Information. The shear moduli of the GelMA and CelMA hydrogels with varying DS are shown in the measured regions of  $0.1$ – $100\text{ rad s}^{-1}$  and the results are given in Figure S3a in the Supporting Information. A decrease in the storage modulus (solid lines) was observed with increasing the degree of methacrylation in GelMA hydrogels, suggesting its viscous properties. The origin of viscous properties in GelMA hydrogels can be attributed to the rapid crosslinking of the randomly arranged polymer chains, causing the nonsignificant enhancement in the elastic properties. Moreover, addition of CNCs in the

polymer matrix facilitates the randomly oriented polymer chains into aligned structures, and strongly interacts with the functional groups of the polymer, leading to the significant enhancement in the storage modulus. CNCs added hydrogels show greater loss modulus (without lines) than the pure polymer. However, their magnitude was lower than the storage modulus, indicating elastic viscoelastic properties. The change in the viscosity complex of the developed hydrogels in the measured regions is presented in Figure S3b in the Supporting Information. The CNCs incorporated hydrogels exhibit improved viscosity complex value than those of the pure polymer hydrogel, elastic properties due the greater interactions between the functionalized polymer chains and added nanomaterial. This was also reflected in the recovery behavior of the CelMA hydrogel. Further, we examined the recovery potential of the hydrogels by measuring the storage modulus at different shear rate and the results are shown in Figure S3c in the Supporting Information. The initial storage modulus was  $1084.1$  and  $1107.07\text{ Pa}$  for CelMA 50 and CelMA 25 hydrogels, respectively, which significantly decreased with increasing the shear strain. However, these hydrogels approximately recovered their initial storage modulus value after removing the high shear strain. The recovered value was  $870.3$  and  $950.98\text{ Pa}$  for CelMA 50 and CelMA 25 hydrogels, respectively. These values were nearly close to the initial, indicating strong recovery efficiency of the hydrogels.

Usually, the rheological properties of a viscoelastic material are independent of strain up to a critical strain level, beyond which the storage modulus declines, leading to the generation of a nonlinear curve.<sup>[21]</sup> We observed that the critical strain ( $\gamma_c$ ) was  $21.17\%$  in the case of GelMA hydrogel, which increased to  $38.24\%$  in the case of CelMA hydrogel, as observed in the strain sweep for the fabricated gels (Figure 1a). The corresponding  $\tan \delta$  values of the fabricated hydrogels were  $27.60$  and  $6.546$  for GelMA and CelMA, indicating the ideal elastic to viscous transition (Figure 1b). To investigate the particle interactions, a frequency sweep at a  $5\%$  strain rate is used and the results are shown in Figure 1c. The elastic modulus ( $G'$ ) was nearly independent of the frequency for the CelMA hydrogel in the measured region, whereas a decrease in  $G'$  was observed for the GelMA hydrogel. This indicates that CelMA hydrogels are mechanically more robust than their GelMA counterparts. Figure 1d shows that loss factor of the CelMA hydrogels had no obvious change within the measured frequency region, indicating its solid like behavior. Conversely, the GelMA hydrogel exhibited a sudden increase in the  $\tan \delta$  value with increasing frequency, suggesting its elastic to viscous nature. Next, we investigated the flow behavior of the developed hydrogels. As shown in Figure 1e, both GelMA and CelMA hydrogels showed a shear dependent viscosity change. We observed an enhancement of viscosity at low shear rate ( $0.1\text{ s}^{-1}$ ), followed by a rapid decrease in viscosity as the shear rate was increased to  $100\text{ s}^{-1}$ . This indicates an ideal shear thinning nature of the fabricated hydrogels. Furthermore, the CelMA hydrogel displayed excellent stress yielding property compared to the GelMA hydrogel which probably arise due to the interaction between polymer matrix with the CNCs resulting in rapid break and rejoining (Figure 1f). We next analyzed the recovery potential of the developed hydrogels under varying shear rate. Notably, the GelMA and CelMA hydrogels maintained the recovery potential around  $\approx 40\%$  and  $\approx 64\%$ , after one cycle. Interestingly,

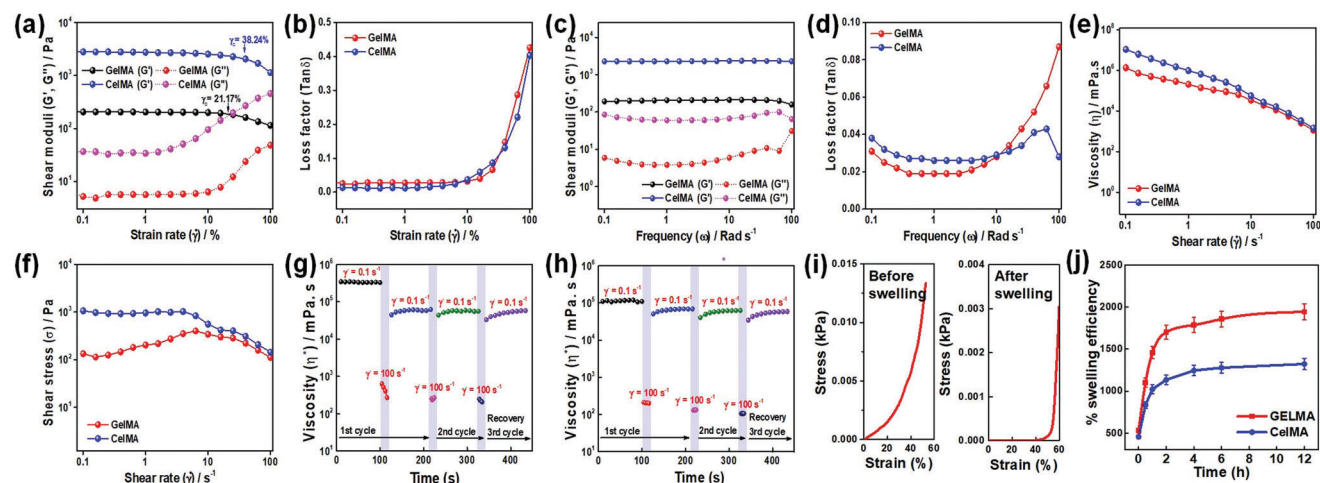


**Figure 1.** Rheological and mechanical characterization of the GelMA and CelMA hydrogels. a,b) Amplitude sweep test with corresponding loss factor calculation of the developed hydrogels within 0.1–100 strain rate; c,d) Frequency sweep test with corresponding loss factor calculation of the developed hydrogels within 0.1–100 Rad s<sup>-1</sup>; e,f) The flow curve (viscosity vs shear rate) and shear stress measurement of the developed hydrogels at RT; thixotropic behavior of the g) GelMA and h) CelMA hydrogels as a function of time with varying shear rate; i) Compressive stress–strain curve of the 3D-printed CelMA hydrogels before and after swelling; j) Swelling efficiency of the fabricated hydrogel scaffolds at indicated time points.

both the hydrogels maintained a recovery potential  $\approx 90\%$  after third cycle, suggesting that both the hydrogel had superior deformation/reformation property (Figure 1g,h). Taken together, our results demonstrated that the fabricated CelMA hydrogel was highly viscoelastic, exhibited superior stress yielding property, and showed desirable criteria for 3D-printing application.

We further examined the swelling property of the fabricated hydrogels, as shown in Figure 1j. The addition of CNC controlled the instant swelling behavior of the scaffold within 1 h of immersion in phosphate-buffered saline (PBS), and the trend continued even after 12 h of PBS immersion, indicating CNCs as physical crosslinkers in the fabricated hydrogel. A tightly interconnected network of GelMA and CNC might restrict the swelling of the hydrogels. Our swelling data are as per the rheological behavior of the CelMA. Based on our results, we chose CelMA hydrogel for further characterization. The mechanical properties of CelMA hydrogel were evaluated before and after swelling. We observed fair retention of the mechanical stability of the CelMA hydrogels for up to 7 days after swelling, as depicted in Figure 1i. The Young's elastic modulus of the CelMA hydrogel was calculated to be  $70 \pm 0.00049$  Pa, making CelMA a soft yet durable hydrogel for the PPS study.

## 2.2. Structural Properties of GelMA and CelMA Hydrogels

Next, we 3D printed the GelMA and CelMA inks using the digital light processing (DLP) printing technology. A schematic of the DLP printing process of the fabricated hydrogels is presented in Figure S4 in the Supporting Information. We printed a  $10 \times 10 \times 5$  mm cubic structure with three internal filaments of 0.8 mm each, as depicted in the sliced computer-aided design (CAD) model. Twenty-five layers were printed for GelMA and CelMA bioinks. A 405 nm UV light source is used to solidify the biomaterial ink via photopolymerization on each layer upon light exposure. We adjusted the layer exposure time for printing the desired

structure while keeping other printing parameters constant. The surface morphology of the printed scaffolds is observed in the field-emission scanning electron microscope (FE-SEM) images in Figure 2a. We observed prominent changes at the microscale level in the CelMA hydrogels w.r.t. its GelMA counterpart. While the GelMA hydrogel showed distinct pockets ( $71.32 \pm 4.99$   $\mu\text{m}$ ) interconnected by relatively thick walls ( $8.551 \pm 0.84$   $\mu\text{m}$ ), the CelMA hydrogels exhibited diffused pores ( $101.05 \pm 15.44$   $\mu\text{m}$ ) interconnected by thin walls ( $2.42 \pm 0.23$   $\mu\text{m}$ ). The difference in the observed morphometric changes is highly indicative of the influence of CNCs in the photopolymerization of GelMA upon UV exposure during the printing process. The photopolymerization of the polypeptide network in the pristine GelMA hydrogel shows a tighter entanglement among the polypeptide resulting in distinct pockets. However, the incorporation of the nanomaterial provides a template for the interaction of the polypeptide with the CNCs beside the interaction among polypeptides. Thus, the presence of CNCs promotes the formation of diffused porous microstructure.<sup>[22]</sup> Moreover, we noticed a homogenous distribution of the major elements in both the scaffolds (Figure S5, Supporting Information). We further analyzed the surface pattern of the fabricated hydrogels at nanometer scale. We observed highly organized fibrillary topography (mean diameter:  $10.525 \pm 1.90$  nm) in the CelMA hydrogels which were not observed in the GelMA counterpart. The presence of CNCs thus provided framework for polypeptide polymerization in a unique pattern at nanoscale. The involvement of CNCs in controlling the nanoscale aligned patterning was confirmed using atomic force microscopy (AFM) images. AFM images representative of each sample are given in Figure 2b. The presence of highly overlapped rod-like nanostructures ( $\geq 42.32 \pm 3.57$  nm) highlighted in the phase images shows the presence of CNCs in bundles. The dotted lines represent the locations on the phase images selected to measure the surface height values at a range of a few nanometers (Figure S6, Supporting Information). An increase in the height profile was observed in the CelMA hydrogel by  $\approx 30$  nm, which

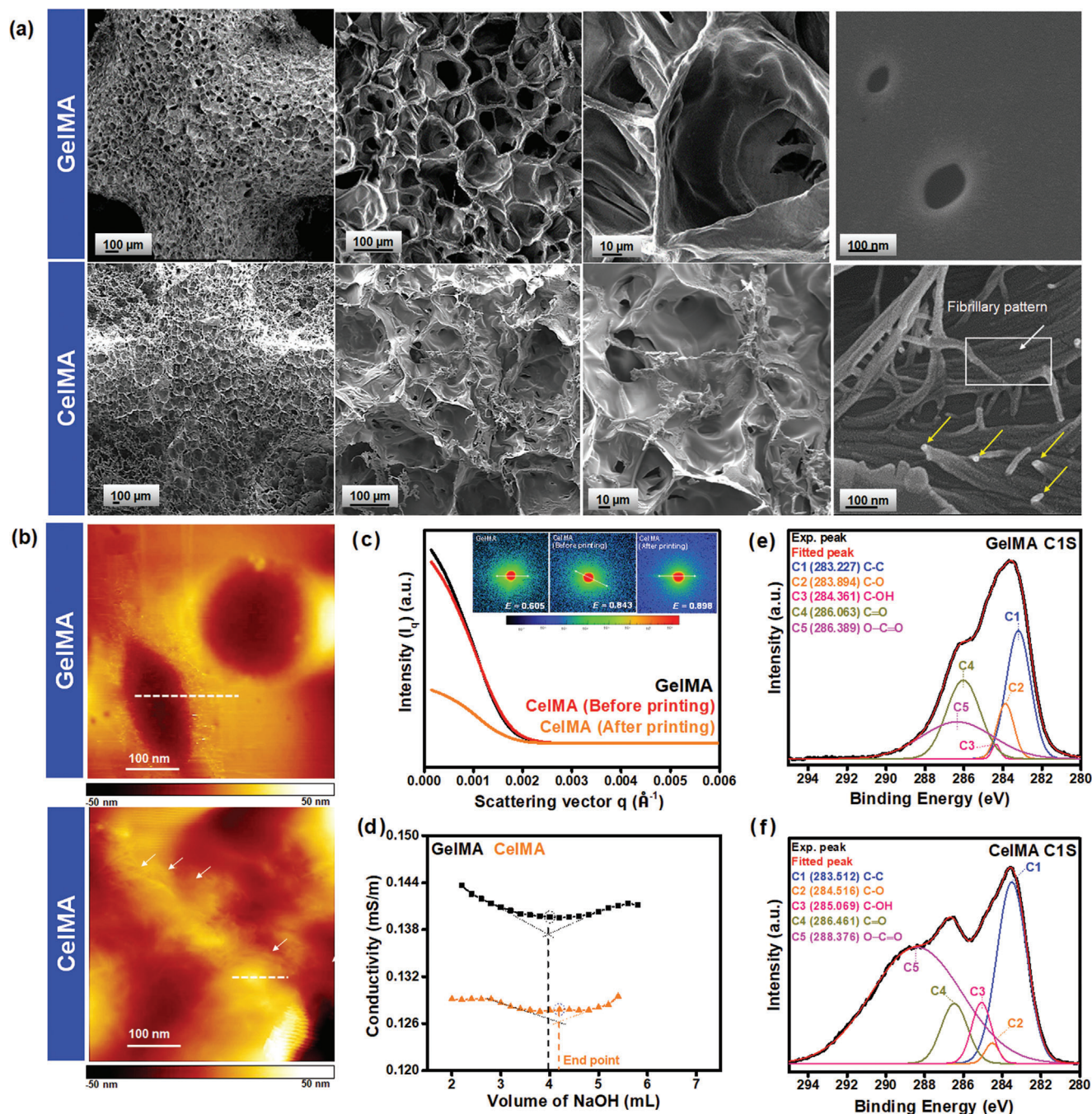


**Figure 2.** Structural properties of the fabricated hydrogels. a) FE-SEM images of the 3D-printed scaffolds showing the porosity and fibrillary network; b) AFM phase images of the fabricated hydrogels; c) SAXS pattern of the GelMA and CelMA (before and after printing) showing the molecular arrangement; d) Estimation of CNC content in GelMA in terms of ionic conductivity; e, f) High-resolution XPS (C 1s) spectra of the GelMA and CelMA hydrogel scaffolds.

is in close proximity to the diameter of the CNCs used in the hydrogel.<sup>[23]</sup> A well distribution of the CNCs was also spotted throughout the scanned region of the CelMA hydrogel. To further analyze the network structure, we performed the small-angle X-ray scattering (SAXS) analysis of the 3D-printed GelMA hydrogel, CelMA suspension, and the 3D-printed CelMA hydrogel as represented in Figure 2c. 3D-printed CelMA hydrogel was found to demonstrate the most elongated 2D profile with an eccen-

tricity value of 0.898. The eccentricity values of GelMA hydrogel and CelMA suspension were 0.605 and 0.843, respectively. The 2D pattern of the fabricated gels clearly indicated anisotropic arrangement in the network structure in the CelMA hydrogel post-printing, indicating pressure-induced self-assembly of the CNCs.<sup>[24]</sup> The corresponding 1D profiles of the 2D SAXS pattern shows similar scattering profile in the GelMA hydrogel and the CelMA suspension. However, a broad hump was obtained in

the scattering profile of the 3D CelMA hydrogel confirming its anisotropy. The content of CNC in the printed hydrogel is a crucial factor determining the overall physio-chemical functionality of the CelMA hydrogel. Hence, we analyzed the CNC content in the printed scaffolds by quantifying the surface charge density in terms of the sulfate and carboxylate contents using the electrical conductivity titration method as shown in Figure 2d. The surface charges in the printed GelMA and CelMA scaffolds were observed to be 54.31 and 56.53 mmol g<sup>-1</sup>, respectively. Additionally, the surface functional groups were also investigated through the X-ray photoelectron (XPS) spectroscopy analysis. The XPS total survey scan of the GelMA hydrogels exhibited survey peaks at 529.010 and 283.913 eV corresponding to O 1s and C 1s, respectively. Whereas, the CelMA hydrogel showed peaks at 529.010 and 286.159 eV for O 1s and C 1s, respectively. The change in the C 1s peak positions might result from the differences in the electronic environment in the hydrogels. To gain an insight into the surface chemical state, high-resolution C 1s scan was performed and the results are displayed in Figure 2e,f. The high-resolution XPS spectrum of the C 1s of the GelMA hydrogel showed a sharp peak and a hump region which could be prominently deconvoluted into five peaks at 283.2 (C–C), 283.8 (C–O), 284.361 (C–OH), 286.063 (C=O), and 286.389 eV (O–C=O). The high-resolution XPS spectrum of the CelMA hydrogel was found to have a broadened hump toward higher binding energy with significant shifts in the peak positions of the functional groups. The high-resolution XPS spectrum of the C 1s of the CelMA hydrogel could also be prominently deconvoluted into five peaks at 283.5 (C–C), 284.5 (C–O), 285.0 (C–OH), 286.4 eV (C=O), and 288.3 eV (O–C=O). We estimate that the shifts in the peak position are induced by the various chemical interactions among the functional groups in the GelMA and CNCs. We measured the changes in the quantity of the functional group by determining the area under the XPS spectrum. The amount of C–C, C–O, C–OH, C=O, and O–C=O in the GelMA hydrogel was measured to be 27.69%, 10.57%, 4.13%, 23.92%, and 23.75%. Whereas, the percentage of the above-mentioned functional groups were observed to be 28.73%, 1.80%, 6.61%, 8.60%, 55.48%, respectively in the CelMA hydrogel. We observed a dramatic decrease in the C–O and C=O content in the CelMA hydrogel by ≈9% and 15%, respectively. While an abundance of O–C=O functional groups was by 27% in the CelMA hydrogel.

### 2.3. Pulsatile Pressure Stimulation on 3D Culture

The customized pulsatile pressure bioreactor system consisted of a vacuum pump double cylinder (35–40 L min<sup>-1</sup> flow, vacuum degree of 650 mmHg) to create the necessary pressure condition, a real-time pressure monitoring and display unit, tubing, one-way valve, 0.25 × 10<sup>-6</sup> m air filter, a rectangular metallic bio-chamber (160 × 120 × 55 mm) capable of accommodating one standard tissue culture plate per pressure stimulation event, immobilized fasteners, and a silicone gasket sealant. Digital photographs of the entire bioreactor setup with PPS are shown in Figure 3a–i. A microprocessor-controlled actuator and pressure valves were used to control the PPS of 5–20 and 20–30 kPa. The bio-chamber comprises an upper lid on top of the lower chamber. The pressure pump received humidified sterilized air from

the incubator and generated the desired pulsatile pressure inside the bio-chamber. The pressure was regulated through the tubing system into and out of the bio-chamber in a unidirectional flow. Filtered air entered the chamber through the inlet and exited through the outlet, exerting an equally distributed pressure on the top of the media containing the cell-hydrogel construct. Thus, pulsatile pressure of the desired amplitude was imparted over the constructs. Pulsatile pressure was applied for 20 min every 24 h to cultured hBMSCs, and the real-time pressure signals were recorded using a pressure manometer operation software as shown in Figure 4a,b.

### 2.4. Biocompatibility Assessment for PPS

Understanding the fact that hydrogel stiffness and GelMA methacrylation degree profoundly affect the cell viability,<sup>[18,25]</sup> we assessed the stiffness of the CelMA hydrogel with varying GelMA DS. The stiffness was monitored in terms of resistivity with varying pressure condition. As shown in Figure S7 in the Supporting Information, the CelMA hydrogel with 71.44 ± 0.32% degree of substitution showed least change compare to its other counterparts, indicating that resistance change in the 71.44 ± 0.32% DS hydrogel is occurring in a controlled way within the measured pressure range. Hence, the CelMA hydrogel with 71.44 ± 0.32% degree of substitution is suitable for the study of osteogenesis on soft hydrogels. Next, we assessed the biocompatibility of hBMSCs on the 3D-printed GelMA and CelMA scaffolds upon PPS at 5–20 and 20–30 kPa for 5 days. hBMSCs cultured on the fabricated scaffolds without PPS served as the control. We observed an enhancement in the viability of cultured cells in the presence of scaffolds with/without (w/wo) PPS. However, under both 2D and 3D culture conditions, exposure to PPS resulted in a noticeable increase in the cell viability after 24 h of stimulation (Figure 4c). Among the GelMA and CelMA hydrogels exposed to mechanical stimulations, we observed a similar trend in hBMSC viability for both hydrogel constructs. Based on our data, we further evaluated hBMSC viability through the live/dead assay on the 3D scaffold w/wo mechanical stimulation after 3 days of culture. Both scaffolds were highly biocompatible, with no visible dead cells observed (Figure S8, Supporting Information). Moreover, we observed a homogenous cell distribution in both the hydrogels without PPS stimulation. However, PPS resulted in the aggregation of the cells indicating the role of contact mechanical pressure upon pressure stimulation at the air–cell–matrix interfaces. Though cell viability was not compromised under any culture condition.

As the cell viability represented a similar trend in the hBMSCs under all the experimental conditions, we chose 5–20 kPa PPS as the pressure condition for analyzing osteogenic differentiation and early transcriptomic changes involved only in CelMA hydrogel. Applying stress to cells often triggers oxidative damage and can inhibit cell differentiation. Hence, we first chose to study the oxidative damage in the hBMSCs upon PPS. For this, we have performed the H<sub>2</sub>O<sub>2</sub>-induced oxidative stress by H<sub>2</sub>DCF-DA staining, as depicted in Figure 4d. A basal level of reactive oxygen species (ROS) production was observed in the negative control set (w/o pressure, w/o H<sub>2</sub>O<sub>2</sub>), indicating physiological ROS production. Similar ROS production was observed in the negative control set upon H<sub>2</sub>O<sub>2</sub> stress, as confirmed in the

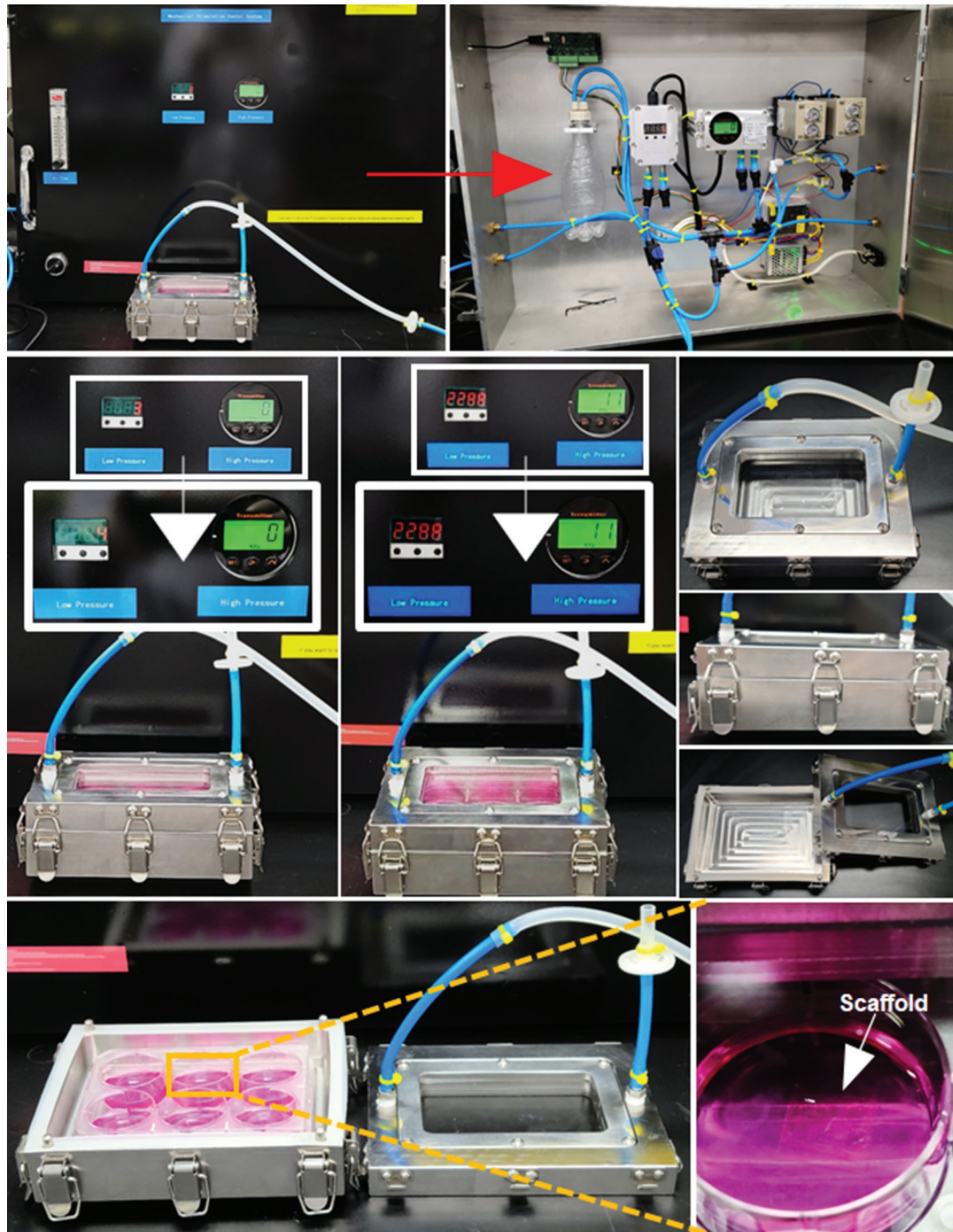


**Figure 3.** Pulsatile pressure bioreactor setup. a) Custom designed pulsatile pressure chamber in a) closed, b) open form. c) The bioreactor operation at 0 kPa pressure. d) The bioreactor operation at 10 kPa pressure. The air pressure was controlled using an external pump. e, f) The assembled cartridge reactor e) top view, f) side view. g) The unassembled cartridge reactor (top view). h) Six-well plate inserted in the cartridge reactor with i) implanted 3D-printed scaffold.

normalized intensities. Unexpectedly, the ROS production was drastically reduced in the PPS-treated cells in the presence or absence of  $H_2O_2$ . To investigate the changes in antioxidant defense system of hBMSCs, we further investigated the gene expression profile of various ROS generating or scavenging gene markers

expression. As shown in Figure 4e, major antioxidative or ROS productive genes such as *SOD2*, *NOX4*, *CAT*, *TXNR1*, and *GPx* family markers were either up- or downregulated in the presence or absence of PPS. The expression of *SOD2*, *CAT*, and *TXNR1* gene markers remained unchanged in the PPS +  $H_2O_2$  group

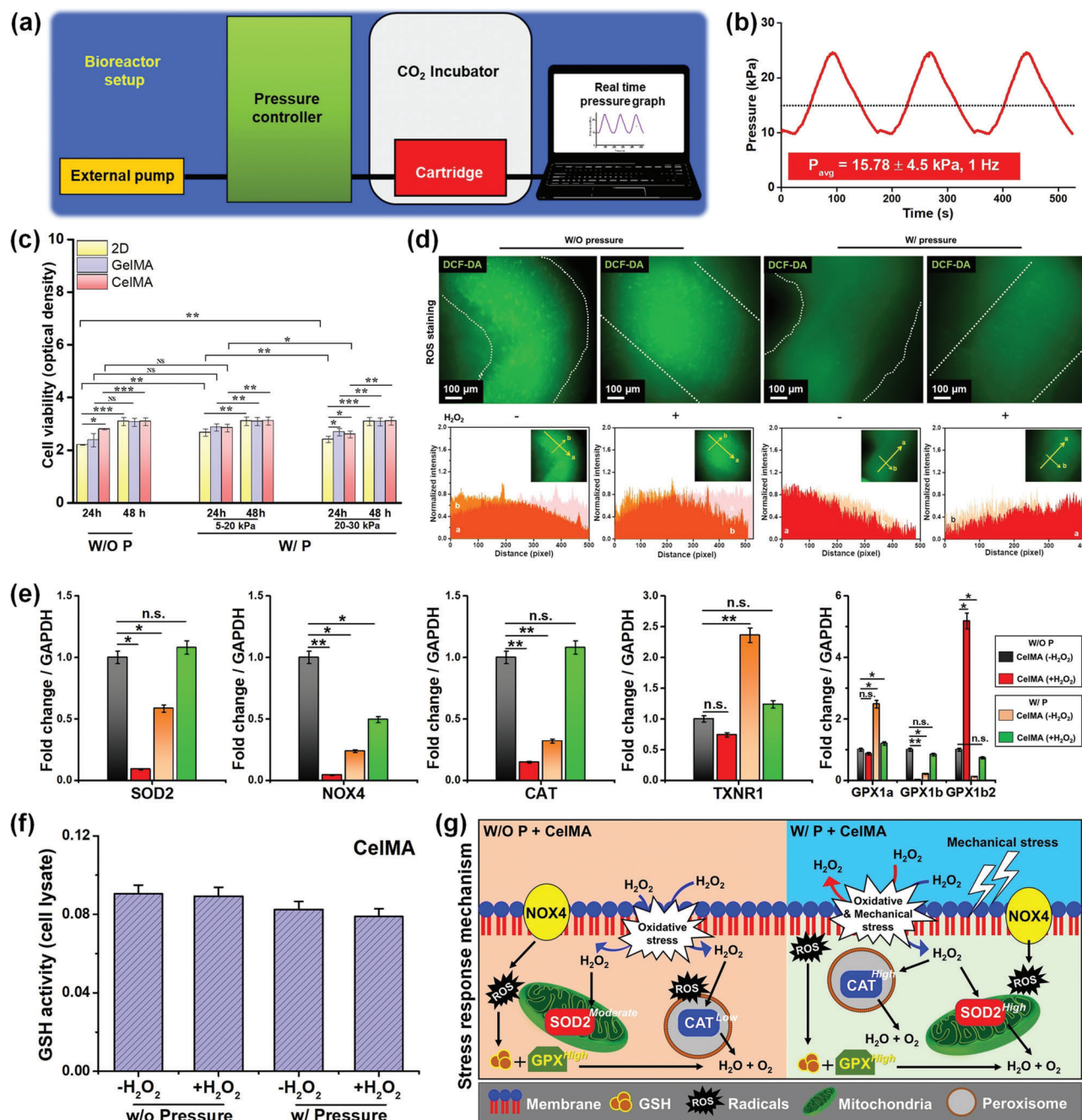


**Figure 4.** In vitro biocompatibility and ROS assessment of the developed hydrogels. a) Schematic illustration of the bioreactor setup. b) Pulsatile pressure stimulation (PPS) graph as recorded using pressure manometer. c) WST-8 assay of the hBMSCs with (w) or without (w/o) PPS at indicated time intervals. d) ROS scavenging assay; green fluorescent images of DCF-DA in hBMSCs after 2 h of incubation following PPS (5–20 kPa) with corresponding intensity profiles. e) qRT-PCR analysis showing the expression of various ROS-sensitive genes in hBMSCs, such as *SOD2* (mitochondrial), *NOX4* (cell membrane), *CAT* (peroxisome), *TXNR1* (cytosolic), and *Gpx* family (cytoplasmic) w/o PPS (20 min stimulation); f) Total GSH activity of hBMSCs w/o PPS (20 min stimulation); g) A hypothetical diagram showing the mechanism of ROS scavenging in the presence of PPS.

compared to the control, suggesting that the ROS generated through  $H_2O_2$  was quickly scavenged. The underlying mechanism of the  $H_2O_2$  scavenging was probably due to the degradation of  $H_2O_2$  onto  $H_2O$  and  $O_2$  via *SOD2* and *CAT* in the mitochondria and peroxisome during PPS.<sup>[26]</sup> Interestingly, the expression of *Gpx* gene family (*GPX1a*, *GPX1b*, and *GPX1b2*) was

significantly decreased following PPS +  $H_2O_2$  treatment. To confirm this, we also investigated the total glutathione (GSH) activity of the hBMSCs during PPS. As shown in Figure 4f, the total GSH level was significantly decreased, which resembles the real-time polymerase chain reaction (qRT-PCR) data. Therefore, we anticipate that the ROS scavenging activity of the hBMSCs in the

presence of PSS was due to the involvement of mitochondrial and other cytosolic factors, and not through the *GPx* pathway.<sup>[27]</sup> A hypothetical diagram showing the PSS-mediated stress response is given in Figure 4g.

Next, we studied the actin cytoskeletal and paxillin distribution using the molecular marker immunostaining to investigate the mechanism of PSS-mediated cell fate commitment on the CelMA hydrogel. We observed well-diffused paxillin distribution in the hBMSCs w/o PSS. Paxillin was strongly expressed at the adhesions upon PSS. Moreover, we observed punctate paxillin distribution at the nuclear periphery in the mechanically stimulated cells (Figure 5a). The paxillin distribution pattern indicated that PSS promoted the formation of matured focal adhesions. The actin distribution was observed to be well organized in the PSS set. We further analyzed the spatial distribution of the actin cytoskeletal protein using the confocal imaging system (Figure 5b). The average spreading area of the actin filaments in the PSS stimulated cells differed sharply from the untreated cells, indicating that the application of the PSS resulted in an increase in the actin signal over 3 days. The PSS-treated hBMSCs exhibited unidirectional actin arrangement, while the untreated hBMSCs displayed diffused actin arrangement. Moreover, most cells were aligned diagonally along the scaffold strand in the mechanically stressed cells. The hBMSCs w/o PSS showed random distribution. Our data strongly suggested that the application of PSS favored a unidirectional alignment of the actin cytoskeleton over the hydrogel surface. Additionally, the nucleus in the control group was observed to be spherical, whereas the cells exposed to PSS showed oblong nuclear morphology, often pushed to the cell periphery. The results indicated that the cells exposed to PSS showed more efficient mechanotransduction compared to the untreated counterparts following PSS.

## 2.5. PSS Accelerates Osteogenic Differentiation of hBMSCs

To investigate the role of PSS in the osteogenic differentiation of hBMSCs, we treated cultured cells in CelMA hydrogel w/wo PSS for 7 days. Following the desired treatment, we determined the early mineralization potential of hBMSCs under the aforementioned conditions using the alizarin red (ARS) staining procedure. Figure 5c (left panel) shows digital photographs of the CelMA hydrogel cultured with hBMSCs for 7 days in osteogenic differentiation media. A light dispersion of mineralized nodule was observed in the hydrogel under the normal atmospheric pressure condition. Under PSS, strikingly increased mineral deposition was recorded in the cells within 7 days of treatment. As a quantitative indicator of the mineralization, we quantified the mineral content in the hydrogels as recorded in Figure S9 in the Supporting Information. An increase in the mineralization was observed in the PSS-treated cells, confirming the more significant mineralization upon PSS. Alkaline phosphatase (ALP) activity in hBMSCs w/wo PSS was also evaluated to further confirm the early osteogenesis in the hBMSCs. Figure 5c (right panel) shows the digital images of the hydrogels and the corresponding optical microscopic images to visualize the ALP expression. We observed a clear increased expression of ALP upon mechanical stimulation. The untreated hBMSCs grew in reticulate fashion

and infiltrated within the CelMA hydrogel. On the other hand, the PSS group displayed a change in cell morphology. The PSS group exhibited elongated and more flattened cell morphology compared to the untreated group. To get a quantitative comparison of the increased expression, we quantified the amount of ALP in the cultured soup. We observed an increase in the ALP secretion by  $\approx 0.5$  mU per 500  $\mu$ L of culture soup (Figure S10, Supporting Information).

## 2.6. Osteoblast-Specific Gene and Protein Expression

To confirm the lineage specification, we next performed the qRT-PCR analysis. As shown in Figure 5d, we used eight osteogenesis-specific gene markers, including *RUNX2*, *ALP*, *Col1*, *BSP*, *OPN*, *OSX*, *RANKL*, and *NF- $\kappa$ B*. We determined the gene expression of early- and late-stage osteogenesis markers in cells under w/wo PSS in 3D culture conditions on day 7. Elevated expression levels of *RUNX2* and *ALP* indicated the onset of osteogenic differentiation of hBMSCs under static and PSS culture conditions. However, both the early phase (*ALP*, *RUNX2*, and *Col1*) and late phase markers (*OSX*, *OPN*, *BSP*) were significantly affected by PSS. Cells cultured under PSS exhibited elevated mRNA levels of *RUNX2* ( $\approx 2.2$ -fold) and *ALP* ( $\approx 15$ -fold) on day 7, which were significantly higher ( $***p < 0.001$ ) than the static samples. However, the expression of *Col1* was reduced upon PSS ( $\approx 0.75$ -fold). It is well known that osteogenic progenitor cells, such as early osteoblasts secrete a low level of *Col1* during bone osteogenesis.<sup>[28]</sup> The expression of *Col1* marker was significantly raised in the later phase of mineralization. Our results showed that *Col1* expression was slightly decreased after 7 days of treatment, meaning that the hBMSCs differentiated into early osteoblast and not the mature osteoblast. Similarly, we observed a dramatic increase in the expression of *BSP* ( $\approx 90$ -fold), *OPN* ( $\approx 40$ -fold), and *OSX* ( $\approx 0.5$ -fold) under mechanical stimulation when compared to static conditions ( $***p < 0.001$  and  $**p < 0.01$ ). Based on the drastic changes in the osteoblast-specific gene expression upon PSS, we further evaluated the expression of *RANKL*, which is crucial in osteogenic differentiation. We observed an  $\approx 28$ -fold increase ( $***p < 0.001$ ) in the expression of *RANKL* in cells exposed to PSS, strongly indicating the more substantial lineage commitment under PSS. The cells' expression of *NF- $\kappa$ B* was equally increased by approximately tenfold ( $*p < 0.05$ ) upon pressure stimulation. We further validated the gene expression results by assessing the expression of selected proteins to check their localization. We confirmed *RUNX2* and *ALP* protein localization after 7 days of cell culture under both conditions (Figure 5e, left panel). Understanding the fact that *MAPK* signaling is one of the crucial mediators of osteogenesis under mechanical stress,<sup>[29]</sup> we further examined the protein expression level of *MEK1* and *ERK1/2*. Notably, both the signaling markers were found highly positive in unstimulated and stimulated groups, suggesting that *MAPK* signaling had significant role during PSS treatment (Figure 5e, right panel). Our immunostaining data confirmed the expression of the osteogenic proteins throughout the cell body, indicating the normal physiological functioning of the hBMSCs under both the culture conditions.

Furthermore, we tested the secretome of the hBMSCs for the detection of cytokines and chemokines and the results are shown

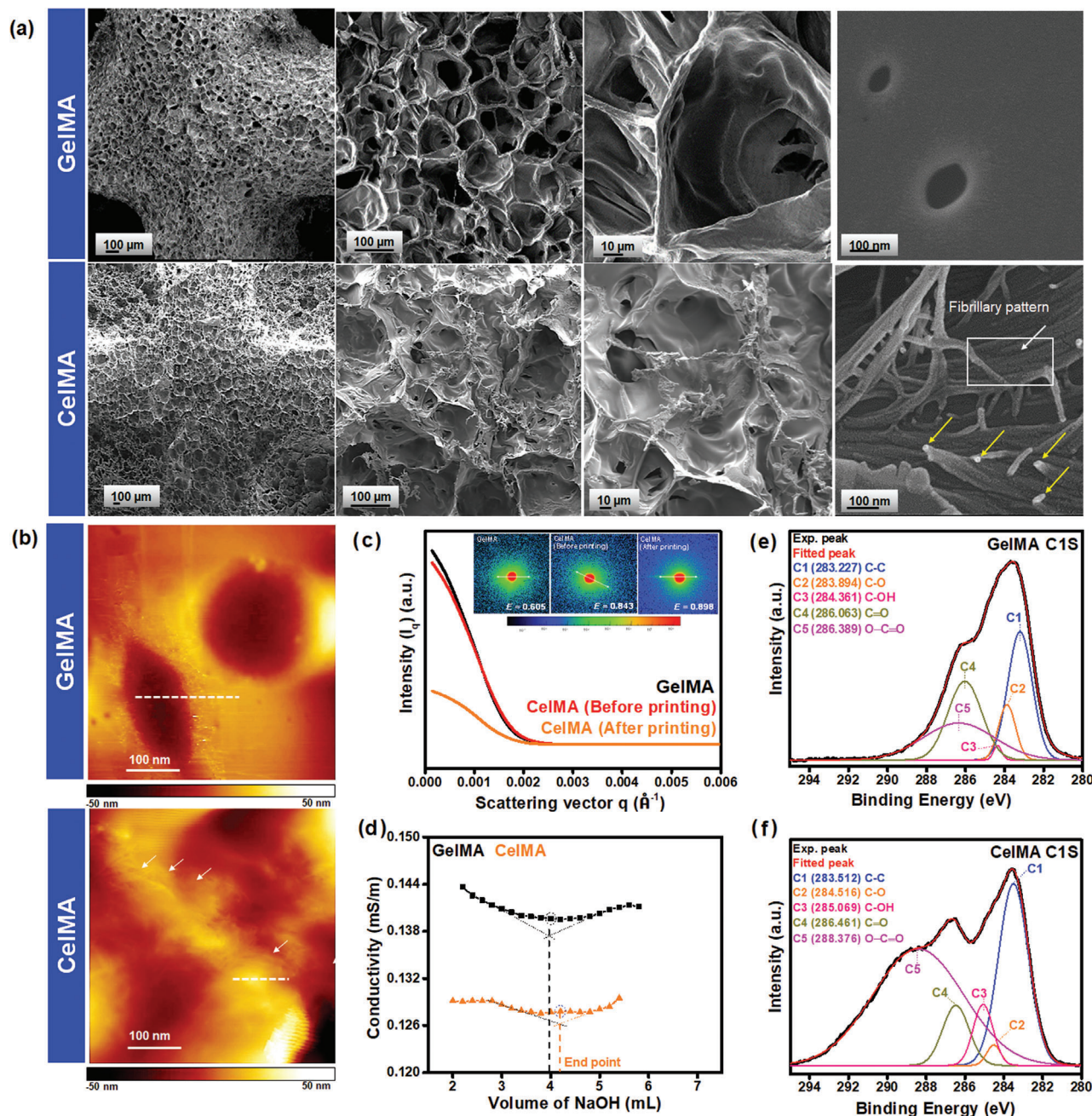


**Figure 5.** In vitro osteogenic potential of the hBMSCs in the presence of CelMA under PPS. a,b) Fluorescent (left panel) and confocal (right panel) microscopic images of the expression of paxillin in the hBMSCs w/o PPS (5–20 kPa); actin (yellow), paxillin (green), DAPI (blue). White arrow indicates the direction of the F-actin orientation; c) Mineralization assay of the hBMSCs w/o PPS using ARS (white dotted line indicates the hydrogel edges); white arrows indicate the mineralization sites) and ALP staining methods (black arrow heads indicate the expressed ALP in hBMSCs) after 7 days of culture; d) Real-time qPCR analysis of the osteogenic marker genes *RUNX2*, *ALP*, *Col1*, *BSP*, *OPN*, *OSX*, *RANKL*, *NF-κB*. e) Fluorescence images of the protein marker expression of osteogenic marker proteins (Runx2 and ALP) and signaling pathway proteins (MEK1 and ERK 1/2). f,g) Secretome analysis of the hBMSCs upon PPS after 7 days of culture with respect to control set. Array membrane with corresponding fold changes of the selected proteins from the supernatant of cultured hBMSCs w/o PPS. Data are mean ± SD of triplicated experiments, statistical significance at \* $p < 0.05$ , \*\* $p < 0.01$ , and \*\*\* $p < 0.001$ . Scale bar: 10 mm, 100, 25, and 20 μm.

in Figure 5f,g. We observed an increase in the secretion of several cytokines, including TGF beta-1, TGF beta-2, OPG (TNFRSF11), IGFBP-2, IGFBP-3, IGFBP-4, IP-10 (CXCL 10), LIF, NT-3, NAP-2, MIP-1 beta (CCL4), IL-6, IL-8, IL-10, RANTES (CCL5), and OSM. In contrast, a reduced secretion was observed concerning

TIMP1 and TIMP2. The last increase was observed in TGF beta-2 ( $\approx 0.8$ -fold), whereas the highest increase was noticed in the secretion of IGFBP-2 ( $\approx 2.8$ -fold). The secretion pattern in the cells upon PPS highly suggests a balance between the expression of osteogenesis-promoting cytokines (TGF beta-1, IGFBP-2,

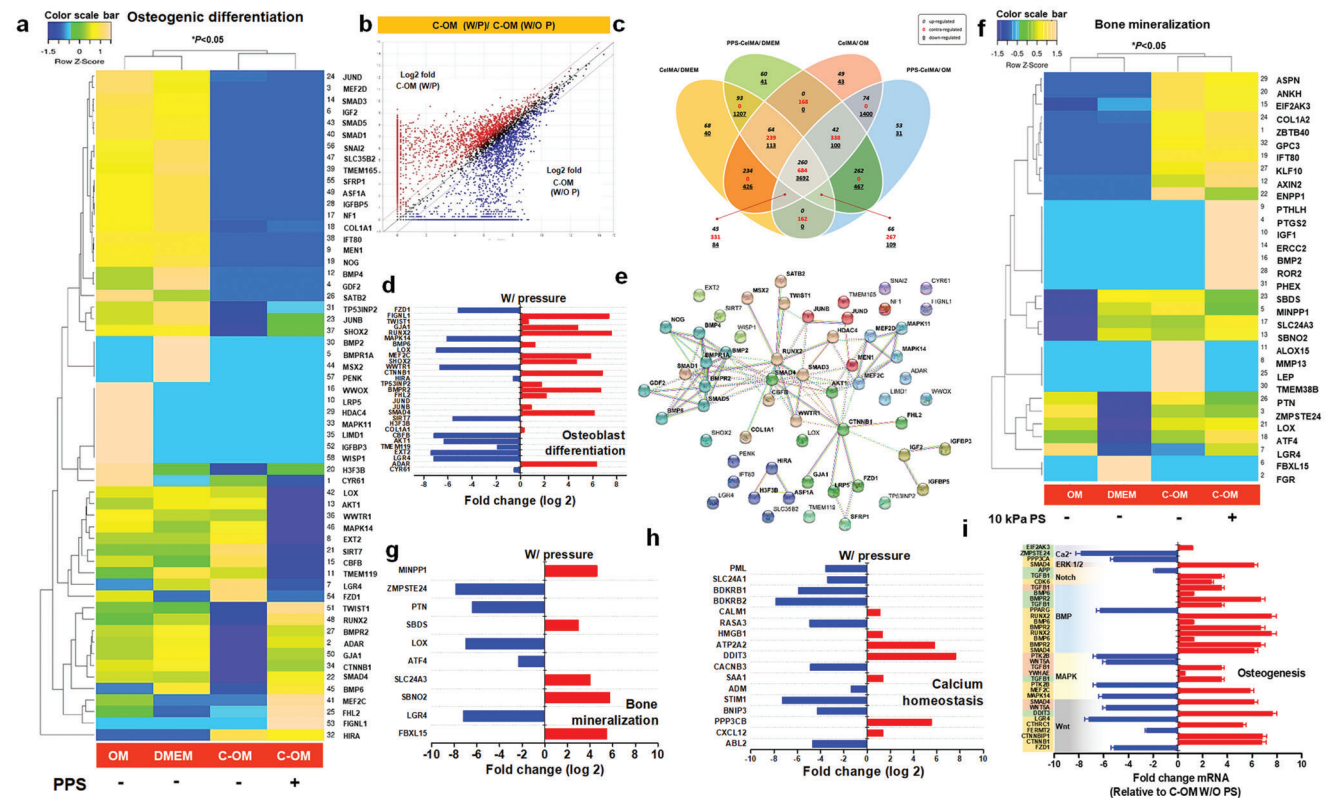


**Figure 6.** Transcriptomic changes in the hBMSCs upon PPS. a) Heatmap of DEGs concerning osteogenic differentiation. Each column represents a sample, and each row represents a gene. b) Pair-wise scatter plot analysis of the changes in gene expression. Each dot (blue, red, black) in the graph represents a gene. Dots along the bisector line are similarly expressed in the two samples compared. Dots further from the bisector indicate higher differential expression. c) Venn diagram of the number of expressed genes in the indicated culture conditions. d) Quantitative plot of the DEGs concerning osteoblast differentiation. e) Protein interaction map of key proteins with high edge confidence of 0.900/1 involved in osteogenic differentiation. f) Heatmap of DEGs concerning bone mineralization. Each column represents a sample, and each row represents a gene. g) Quantitative plot of the DEGs concerning bone mineralization. h) Quantitative plot of the DEGs concerning calcium homeostasis. i) DEGs involved in the osteogenic differentiation upon mechanical stimulation and their placement in the cell signaling pathway. Data are mean  $\pm$  SD of triplicated experiments, statistical significance at  $*p < 0.05$ .

IGFBP-4, NT-3, NAP-2, MIP-1 beta or CCL4, IL-6, IL-8, RANTES (CCL5), OSM) as osteogenesis maintenance cytokines (TGF beta-2, OPG (TNFRSF11), IGFBP-3, IP-10 (CXCL 10), LIF, IL-10).<sup>[28,30]</sup> These results suggest that PPS to CelMA hydrogels can promote osteogenic differentiation within 7 days. We chose to perform a successive evaluation of early transcriptomic changes during PPS using RNA-seq analysis based on our findings.

### 2.7. Comparison of DEGs under PPS on CelMA Hydrogel

The RNA-seq data revealed that 25 737 transcripts were detected with a twofold change (FC) in the expression level concerning the control condition. Based on the differentially expressed genes (DEGs), the most downregulated and upregulated genes were selected for data analysis. The DEGs were subjected to hierarchical clustering and are represented as heatmaps (Figure 6a). We analyzed the expression of genes involved in the osteogenic differentiation of hBMSCs. The scatter plot of gene expression demonstrates the drastic changes in expression patterns under different culture conditions, indicated by the dots lined further from the bisector (Figure 6b,c). Fifty-four genes related to osteogenic

differentiation were observed to be differentially expressed. For simplicity, herein, we have discussed a few genes involved in the commitment of hBMSCs to osteoblast cells and early osteogenesis. Runx2 and BMP6 act as markers for the commitment of MSCs to osteoprogenitor cells.<sup>[31]</sup> We observed a drastic increase in the expression of Runx2 (approximately sevenfold) and BMP6 ( $\approx 1.2$ -fold) in cells upon PPS, clearly indicating that mechanical stimulation on a soft hydrogel can accelerate the differentiation of hBMSCs into osteoprogenitor. We further evaluated the DEGs for a few osteoprogenitor markers, including ALP, collagen I A1 (Col1A1), Osterix (Osx or Sp7), and Thrombopoietin (Tpo). We observed an  $\approx 0.3$ -fold higher expression of Col1A1 in mechanically stimulated cells on CelMA; the expression was downregulated fourfold in cells cultured on CelMA without pressure stimulation. Strikingly, no differential expression was observed for ALP, Sp7, and Tpo. One of the main differences in the expression was for JunD. Deletion of *JunD* is known to increase bone mass by increasing the expression of Fra1, Fra2, and c-Jun, indicating that JunD is a negative regulator of osteogenesis.<sup>[32]</sup> Our data showed a downregulated JunD expression in the presence of osteogenic media, and JunD expression was further downregulated under the 3D culture condition. However, the gene

expression was 0.54-fold downregulated upon mechanical stimulation, whereas the downregulation was  $\approx 1.28$ -fold without pressure stimulation. This indicated that pressure stimulation slightly increased the expression of JunD in cells cultured on the CelMA scaffold (Figure 6a,d). String analysis of all DEGs was performed to determine the clustering pattern. We found a minimum of ten clusters that were actively involved in osteogenic differentiation, indicating the strong physiological response of the hBMSCs toward osteogenic differentiation (Figure 6e).

We then analyzed the DEGs involved in the process of bone mineralization. A total of 32 essential genes involved in bone mineralization were differentially expressed. Interestingly, most genes were overexpressed in the CelMA group upon pressure stimulation compared to their control counterparts. Increased expression was observed for Col1A2 and BMP2. The expression of the genes involved in calcium homeostasis is shown in Figure 6f,g. The genes were clustered in nine groups based on their functional similarity in calcium homeostasis. Cluster analysis of the proteins involving the DEGs revealed nine gene clusters based on their functional similarity in calcium homeostasis (Figure 6h and Figure S11, Supporting Information). The RNA-seq data consisted of in vitro mineralization data using the ARS staining method for mineralization after 7 days of stimulation. Our results suggest that mechanical stimulation of soft hydrogels can stimulate the osteogenic differentiation of hBMSCs within 5–7 days. We checked gene expression changes in several signaling pathways related to osteogenic differentiation (Figure 6i). For simplicity, we chose DEGs that play significant roles in the signal transduction pathway during osteogenic differentiation. DEGs were observed in Wnt, MAPK, BMP, Notch, ERK 1/2, and Ca<sup>2+</sup>-mediated signaling pathways related to osteogenesis. Eight DEGs were observed among the genes associated with the Wnt pathway. The following three significant genes were upregulated: *CTNNB1* (approximately sixfold), *CTNNBIP1* (approximately sixfold), and *CTHRC1* (approximately fivefold). At the same time, the downregulated genes included *FZD1* (approximately fivefold), *FERMT2* (approximately threefold), and *LGR4* (approximately sevenfold). An approximately sevenfold upregulation was observed in *DDIT3* expression, and an approximately fivefold downregulation was observed in *WNT5A* expression; both are actively involved in calcium homeostasis. DEG analysis for genes involved in the MAPK signaling pathway revealed the presence of nine DEGs, of which four were associated with osteoblast differentiation (*SMAD4*, *MAPK14*, *MEF2C*, and *PTK2B*), and one was found to be involved in bone mineralization (*TGFB1*), and four genes were involved in calcium homeostasis (*YWHAE*, *TGFB1*, *WNT5A*, and *PTK2B*). The upregulated genes included *SMAD4* (approximately sevenfold), *MEF2C* (approximately sixfold), *YWHAE* (approximately onefold), and *TGFB1* (approximately fourfold). On the other hand, *MAPK14* and *PTK2B* were downregulated by approximately sevenfold each. Seven genes involved in the process of BMP-associated osteoblast differentiation (*SMAD4*, *BMPR2*, *BMP6*, *RunX2*, *BMPR2*, *BMP6*, and *PPARG*) were observed; three genes involved in bone mineralization (*TGFB1*, *BMPR2*, *BMP6*) and one gene involved in calcium homeostasis (*TGFB1*) were also observed. Three DEGs were involved in osteogenic differentiation (*CDK6*) and bone mineralization (*TGFB1* and *APP*) via the Notch signaling pathway. *SMAD 4* involved in osteoblast differentiation via the ERK 1/2

was upregulated. Three genes were associated with Ca signaling in osteogenic differentiation (*PPP3CA*) and bone mineralization (*ZMPSTE24* and *EIF2AK3*).

We focused on the expression profile of ion channel activity (Figure 7a,b). Osteoblasts and osteoprogenitor precursor cells possess numerous ion channels, including Na<sup>+</sup>, L-type Ca<sup>2+</sup>, volume-sensitive Cl<sup>-</sup>, and mechanosensitive cation channels. Membrane stretch is known to activate the expression of key ion channels, including Piezo 1, Piezo 2, and KCNK2, among others.<sup>[33]</sup> We analyzed the following six key ion channels: Piezo 1, Piezo 2, KCNK2, TRPA, LRRC8A, and TTYH3. The activity of most ion channels was downregulated in 3D cultures without pressure stimulation. However, the application of pressure restored ion channel expression, similar to that observed under 2D culture conditions. Piezo 1 is expressed early during the differentiation of MSCs into osteoblast progenitors, while Piezo 2 is generally induced during osteoclastogenic differentiation. We found that hBMSCs cultured on the 2D surface in the OM showed higher expression of both Piezo 1 and Piezo 2, among which Piezo 2 had the highest expression. hBMSCs cultured on CelMA scaffolds without pressure stimulation showed a drastic reduction in the expression of *PIEZO1* and *PIEZO2* by  $\approx 1.5$ -fold and  $\approx 0.8$ -fold, respectively. However, the application of pulsatile pressure restored the expression of both genes closer to that observed under the 2D-OM culture condition, indicating pressure-induced activation of Piezo expression. We hypothesized that reduced expression indicates negative regulation of osteogenic differentiation.<sup>[34]</sup> However, the downregulation of Piezo 1 has previously been shown to not significantly affect the osteogenic differentiation of stem cells and progenitor cells.<sup>[35]</sup> The expression of leucine-rich repeat-containing protein 8A (LRRC8A) significantly increased under pressure stimulation. LRRC8A is a volume-regulated anion channel (VRAC) essential for hypotonicity-induced iodide influx.<sup>[36]</sup> We envisage that applying pulsatile pressure somehow challenges alterations in the cell volume; however, further evaluation is required. We also observed enhanced expression of calcium-activated potassium channel subunit beta-3 (KCNMB3). KCNMB3 expression has been associated with osteoblast differentiation. The pressure-induced increase in KCNMB3 expression indicated the involvement of Ca<sup>2+</sup>-dependent signaling upon mechanical stimulation.<sup>[37]</sup> The potassium channel subfamily K member 2 (KCNK2), which is responsible for passive transmembrane potassium transport, is another mechanosensitive ion channel. We observed a downregulated expression of this ion channel in the presence of the CelMA scaffold w/o pulsatile pressure stimulation. Thus, our study has revealed that pulsatile pressure mechanical stimulation induces higher expression of Ca<sup>2+</sup> ion channels while reducing the expression of K<sup>+</sup> channels.

We analyzed the transcriptomic changes related to cell adhesion. Several genes like Integrin-linked kinase (ILK) mediate the transmission of information from the extracellular matrix (ECM) to the actin cytoskeleton during bone formation.<sup>[38]</sup> We observed an  $\approx 1.4$ -fold increase in ILK expression in the treatment group (Figure 7c,d). Other critical genes upregulated under PPS included *TNS2*, *ACTN4*, *PXN*, *ITGBL1*, *ITGA3*, *VCL*, *ITGB5*, *ITGA4*, *TNS3*, and *TLN2*.

Downregulated genes under PPS included *ITGB1BP1*, *ITGA5*, *ITGB1*, *TLN1*, and *ITGAS*. Among the genes involved

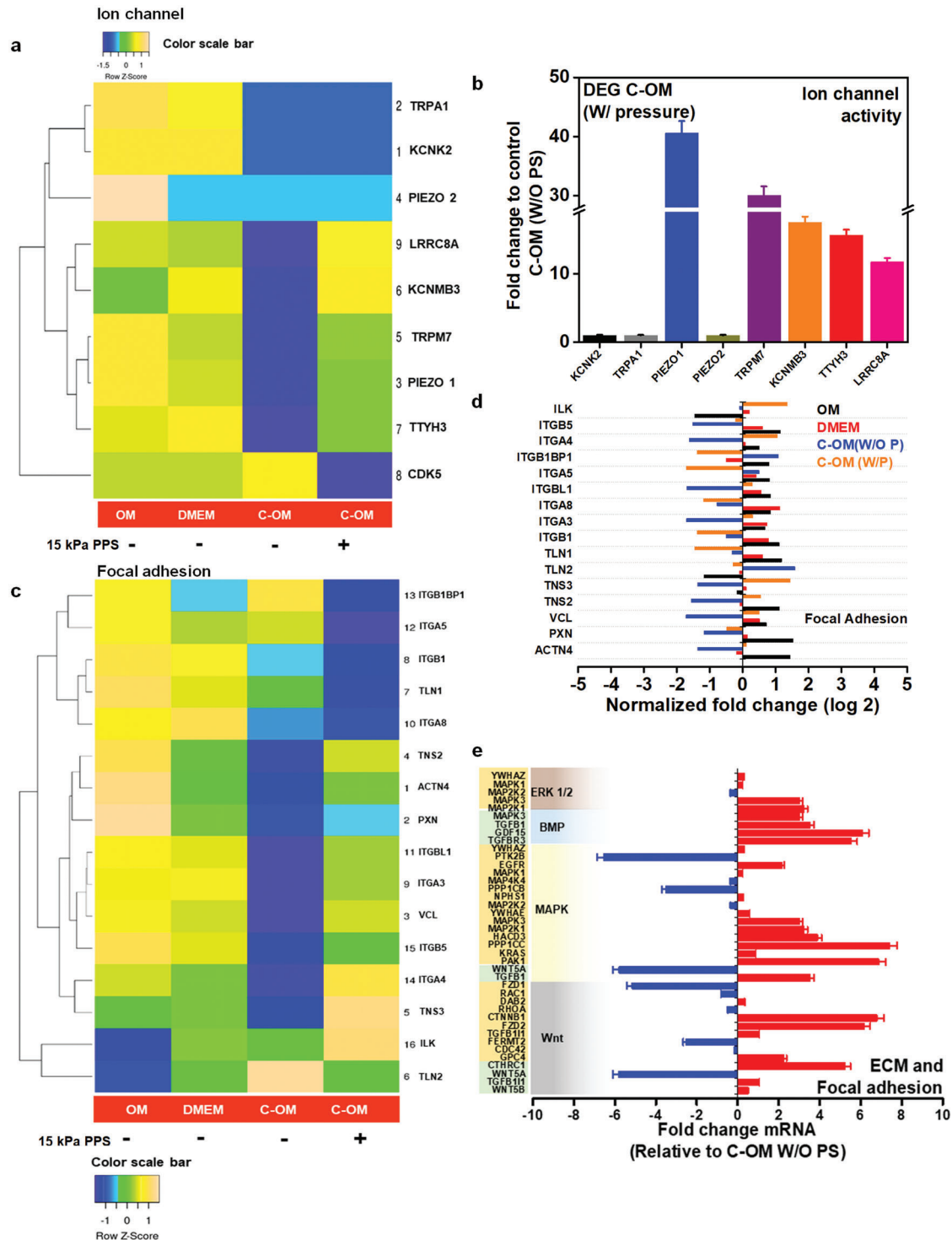


**Figure 7.** Transcriptomic changes in the hBMSCs upon PPS. a) Heatmap of DEGs concerning ion channel expression. Each column represents a sample, and each row represents a gene. b) Quantitative plot of the DEGs concerning ion channel expression. c) Heatmap of DEGs concerning focal adhesion. Each column represents a sample, and each row represents a gene. d) Quantitative plot of the DEGs concerning focal adhesion. e) DEGs involved in the extracellular matrix (ECM) and focal adhesion upon mechanical stimulation and their placement in the cell signaling pathway. OM: osteogenic media; DMEM: cell culture media; C-OM (w/o P): CelMA-osteogenic media without pressure stimulation, C-OM (w/P): CelMA-osteogenic media with pressure stimulation.

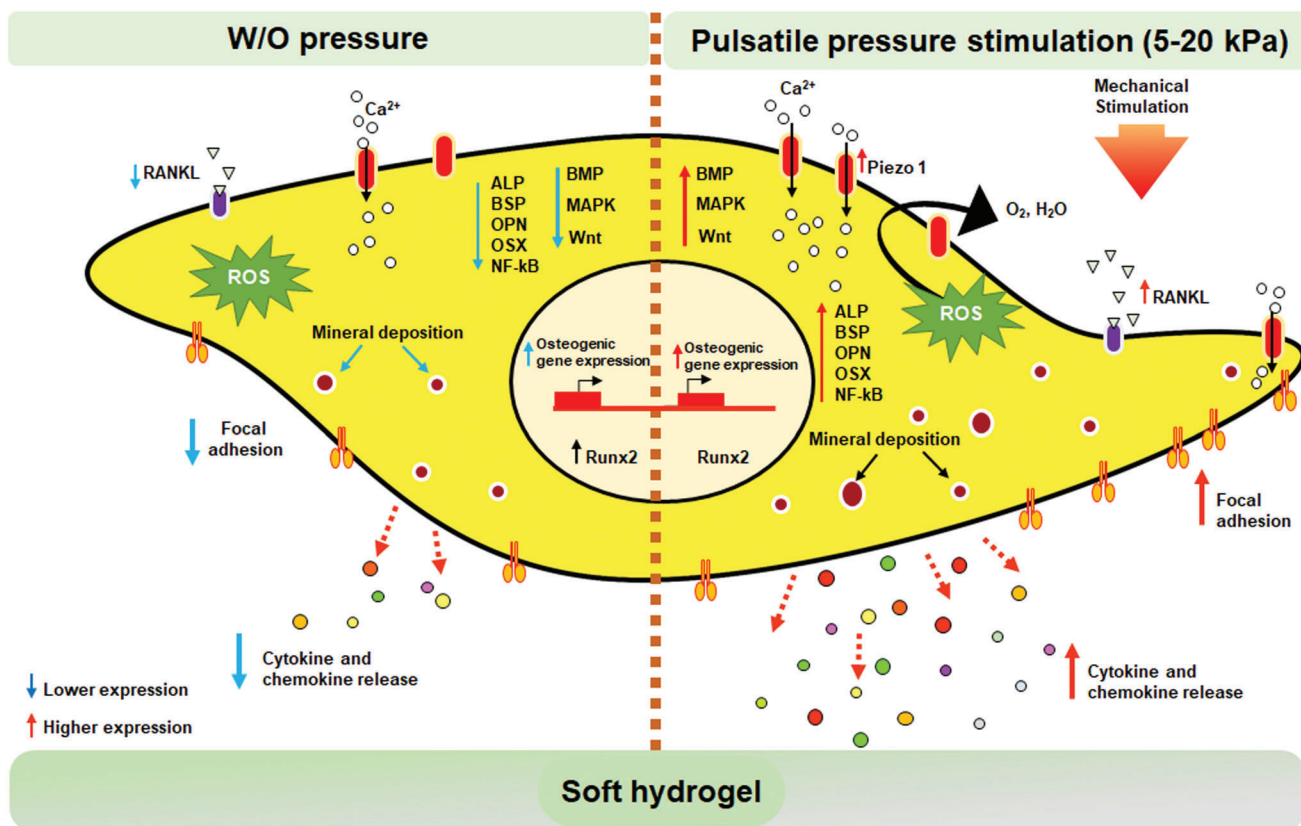


**Figure 8.** Schematic illustration of the changes in the cell physiological behavior w or w/o PPS. RANKL: Receptor activator of nuclear factor Kappa-B ligand; ROS: reactive oxygen species, *ALP*, *BSP*, *OPN*, *OSX*, *NF-kB* represent osteogenesis specific genes; *BMP*, *MAPK*, *Wnt* indicate the intracellular signaling pathways altered upon mechanical stimulation. The blue downward arrow indicates lower expression in the control sample; the red upward arrow represents higher expression in the hBMSCs upon mechanical stimulation.

in focal adhesion, the application of PPS restored the expression of most genes that were downregulated in the CelMA scaffold without pressure stimulation.<sup>[39]</sup> The expression of actin 4, paxillin, and vinculin was enhanced in hBMSCs cultured on CelMA upon PPS by approximately twofold, 0.5-fold, and threefold, respectively. The DEGs involved in focal adhesions in cells under mechanical stimulation. DEGs involved in the formation of ECM included *WNT5B*, *TGFB1/1*, *WNT5A*, *CTHRC1*, *GPC4* (*Wnt* pathway), *TGFB1*, *WNT5A* (*MAPK* pathway), *TGFBFR3*, *GDF 15*, and *TGFB1* (*BMP* pathway). DEGs involved in focal adhesion through the *Wnt* pathway included *CDC42*, *FERMT2*, *TGFB1/1*, *FZD2*, *CTNBN1*, *RHOA*, *DAB2*, *RAC1*, and *FZD1*. Additionally, DEGs involved in *BMP* signaling included *MAPK3*. The *MAPK* signaling pathway showed differential expression of *PAK1*, *KRAS*, *PPP1CC*, *HACD3*, *MAP2K1*, *MAPK3*, *YWHAE*, *MAP2K2*, *NPHS1*, *PPP1CB*, *MAP4K4*, *MAPK1*, *EGFR*, *PTK2B*, and *YWHAZ*. DEGs related to ERK 1/2 included *MAP2K1* and *MAPK1*, while those related to ERK 1/3 and ERK 1/4 included *YWHAZ* and *MAPK3*, and *MAP2K2*, respectively (Figure 7e). A list of DEGs involved in the *Wnt* and *MAPK* signaling pathways is listed in Tables S2 and S3 in the Supporting Information.

To further investigate the cellular processes altered by PPS, we examined DEGs involved in ROS, ER stress, and mitochondrial metabolic processes. The DEGs involved in the ROS metabolic

pathway support our antioxidative assay confirming PPS-induced antioxidative changes. Most genes were downregulated under pressure-stimulated culture conditions, indicating that mechanical stimulation prevented cell stress. Superoxide dismutase 2 (*SOD2*) was upregulated by approximately onefold under the PPS condition. *SOD2* is a crucial enzyme for converting superoxide into oxygen and hydrogen peroxide. Increased expression of *SOD2* may indicate that mechanical stimulation might trigger higher cellular metabolism.<sup>[40]</sup> Nicotinamide nucleotide transhydrogenase (*NNT*), involved in the mitochondrial redox balance, was upregulated by approximately twofold, indicating a higher metabolic activity during the differentiation process (Figure S12, Supporting Information). A schematic diagram showing the effects of PPS on hBMSCs differentiation is shown in Figure 8. Taken together, our results demonstrated that the PPS onto a soft hydrogel matrix made up of GelMA and CNCs may serve as a promising platform for studying early osteogenesis, which would be beneficial for bone tissue-related disease management in the future.

### 3. Discussion

Soft hydrogel technology has been beneficial in treating many critical diseases; however, its limited application in BTE results from the inability of soft hydrogels to promote sufficient surface

stiffness for osteogenic differentiation of stem cells. Establishing a way to utilize soft hydrogels in bone regeneration can greatly support crucial medical conditions like bone marrow mimicking hydrogel development. This work provided a method to manipulate hBMSCs to undergo osteogenic commitment on super soft hydrogel ( $70 \pm 0.00049$  Pa). Our strategy included the application of PPS on hBMSCs at a range of 5–20 kPa ( $P_{\text{avg}} = 15.78 \pm 4.5$  kPa), resembling the physiological medullary pressure generated inside bone marrow ( $\approx 10$  kPa). We envision that this technique will be a valuable addition to the knowledge of promoting osteogenesis in soft hydrogels since methods to achieve osteogenesis on hydrogels as soft as a modulus of  $70 \pm 0.00049$  Pa (elastic modulus) have not been deeply studied.

Load bearing has been shown to enhance intramembranous and endochondral osteogenic differentiation of MSCs, the most crucial process in bone regeneration, under several studied conditions.<sup>[41]</sup> Under natural physiological conditions, bone is usually exposed to constant loading, which is necessary to maintain tissue integrity.<sup>[13]</sup> For instance, the medullary pressure generated inside the bone marrow is  $\approx 10$  kPa, whereas the pressure generated within the lacunar canalicular system is  $\approx 300$  kPa under natural physiological conditions. Cells also constantly receive mechanical stimuli such as stress, strain, fluid flow, and forces generated by cellular interactions. The perception of external mechanical cues and subsequent downstream signal transduction in MSCs also regulate bone growth and development.<sup>[42]</sup> Bone deformation can significantly disrupt physiological pressure balance in the tissue environment. Hence, bone implants combined with mechanical stimulation of the desired amplitude, modality, and duration have promising opportunity for bone treatment.

Numerous pressure bioreactor systems have been developed to construct tissue-engineered bone grafts, including load-bearing fluid flow shear stress-based bioreactors, ultrasound bioreactors, compression bioreactors, tension bioreactors, nanovibrational bioreactors, and multimodal bioreactors, which accelerate bone regeneration for bone graft fabrication.<sup>[43]</sup> While the pressure-induced osteogenic commitment of human bone marrow-derived mesenchymal stem cells (hBMSCs) on a 2D substrate has been highly dependent on the ECM rigidity, 3D platforms have further revealed the role of scaffold dimensionality. MSC osteogenesis in 3D alginate polymers under pressure stimulation has been reported to occur at  $\approx 11$ – $30$  kPa, while 3D soft hydrogels (Young's moduli,  $E \approx 0.6$ – $1.0$  kPa) were observed to stimulate cell proliferation with cells exerting traction stresses of 0.1–5 kPa on the ECM. MSCs seeded on collagen-coated silicone substrates, upon exposure to tensile mechanical uniaxial strain (2.5% at a rate of 0.17 Hz), have been shown to express a fivefold higher BMP2 level after 14 days of stimulation. This effect has been reported to occur via the ERK and PI3-kinase pathways. Methacrylate gelatin (GelMA), owing to its resemblance to collagen in native ECM tissues, good thermal sensitivity, and photocrosslinking ability, has been extensively used in the fabrication of 3D-printing bioinks.<sup>[44]</sup> CNCs have been shown to induce osteogenesis. Regardless of the establishment of 3D scaffolds, biomimicking the native conditions of MSCs osteogenic differentiation requires dynamic mechanical strain crucial for regenerating functional connective tissue. Thus, substrate mechanics is a specific determinant factor for the generation of bone grafts under mechanical stimulation. The current understanding of the

mechanism that integrates external pressure stimuli with the genetic regulation of osteogenic differentiation remains largely unclear. In addition, the role of transcriptomic changes resulting from the combined effect of substrate mechanics and mechanical loading in determining the fate of hBMSCs remains to be elucidated.<sup>[45]</sup> Our custom-designed pulsatile pressure bioreactor system generated 5–20 kPa pressure stimulation to hBMSCs and studied the transcriptomic changes relevant to bone regeneration through RNA-sequencing. We found that PPS of 5–20 kPa on CelMA hydrogel triggers osteogenic differentiation of hBMSCs through the alteration of numerous cell physiological processes, including differential expression of osteogenic specific genes, membrane proteins, and cytokine release.

## 4. Conclusion

In this study, we analyzed the critical contribution of short-duration pulsatile pressure mechanical stimulation of 5–20 kPa (with an average of  $15.78 \pm 4.5$  kPa) toward the osteogenic differentiation of hBMSCs on soft hydrogel ( $70 \pm 0.00049$  Pa). We found that a pulsatile pressure increased osteogenesis in hBMSCs involving cellular responses including cell adhesion, proliferation, apoptosis, bone mineralization, calcium homeostasis, ion channel regulation, and reduced oxidative stress. We confirmed that pulsatile pressure stimulation significantly promotes osteogenic differentiation within 7 days of stimulation and hence, can be utilized for bone regeneration processes, generation of in vitro bone grafts, and fabrication of medical devices.

## 5. Experimental Section

**Materials:** CNCs from cotton pulps (10–20 nm width, 50–400 nm length; 12% solid content; crystalline index:  $>70\%$ ), Gelatin type A powder from porcine skin (purity:  $\geq 98\%$ ; gel strength  $\approx 300$  g bloom), lithium phenyl-2,4,6-trimethylbenzoylphosphinate (LAP), and MAA were purchased from Sigma-Aldrich, St. Louis, MO, USA. Dulbecco's modified Eagle's medium (DMEM), 10% fetal bovine serum (FBS), Dulbecco's PBS (DPBS), and antibiotics were purchased from Welgene Inc., Republic of Korea. Trypsin-ethylene diamine tetra acetic acid (Trypsin-EDTA) was provided by Gibco, USA. Osteo-induction media, 4,6-diamino-2-phenylindole dihydrochloride (DAPI), and ARS staining kit were acquired from Sigma-Aldrich, USA. WST-8 dye (EZ-Cytox Cell Viability Assay Kit) and Alexa Fluor conjugated monoclonal antibodies were purchased from DoGenBio Co., Ltd., Republic of Korea, and Santa Cruz Biotechnology, USA, respectively. TRIZOL reagent, Acridine orange, and ethidium bromide stains were purchased from Invitrogen, Thermo Fisher Scientific, USA. The cDNA synthesis kit was obtained from Invitrogen, Gaithersburg. SYBR Green Master mix was supplied by Bio-Rad Laboratories, USA. The gene primers were supplied by BIONEER Inc., Daejeon, Republic of Korea.

**Bioreactor Design:** The costumed designed bioreactor system consisted of a pressure control unit (low, 0–100 Pa and high, 0–100 kPa), a vacuum pump double cylinder ( $35$ – $40$  L  $\text{min}^{-1}$  flow, vacuum degree of 650 mm Hg), and a rectangular metallic cartridge chamber ( $160 \times 120 \times 55$  cm) to hold the well plate for pressure stimulation on cultured cells. The air pressure was controlled using an external pump and the installed air tank with a capacity of 2000 mL. The real-time pressure stimulation was recorded using a BENETECH pressure manometer.

**Bio-Ink Formulation: Synthesis of GelMA:** GelMA foam was synthesized following previous reports. Briefly, 10 g of Type A gelatin was dissolved in 100 mL sterile PBS (pH 7.4), followed by the addition of 0.25, 1.25, and 1.6 mL of MAA with continuous stirring at 40–45 °C for 2 h. After 2 h, the reaction was stopped by adding twofold warm PBS and

stirring for 10 min. The resulting solution was dialyzed against sterile distilled water using a dialysis tube (12–14 kDa cutoff molecular weight) for 5–7 days to remove the methacrylic acid. Next, the GelMA solution was concentrated and lyophilized for 7 days to obtain a white foam and stored at  $-80^{\circ}\text{C}$  until use. GelMA-CNC ink was prepared as follows. Briefly, 12% (vol%) GelMA was dissolved in DW at  $40^{\circ}\text{C}$ , followed by adding 2% CNC (w.r.t. GelMA) until a homogenous solution was obtained. Next, 0.25% photoinitiator (LAP) was added to the GelMA-CNC hydrogel solution. The hydrogels were carefully (without forming air bubbles) used for 3D printing.

**DLP Printing:** The  $10 \times 10 \times 5$  mm structures were designed by the Solid works software (www.solidworks.com, Dassault Biosystems, France) and exported as STereoLithography (STL) file. Before fresh printing, all the STL files were sliced using custom-designed Slicer software (Carima Slicer, v2.0.3, Republic of Korea). The printable resin was directly used as a vat for the DLP printing. The DLP printer was equipped with a UV digital mirror device (DMD) of 405 nm UV-light-emitting diode with an average intensity of 400 lumens, build resolution (XY) was  $1920 \times 1080$  mm (engine resolution), and the build size (XYZ) was  $96 \times 54 \times 150$  mm, respectively. The z-axis thickness and pixel size were set at 0.1 mm per layer and 50  $\mu\text{m}$ . The overall dimension of the printer was  $300 \times 320 \times 650$  mm, respectively. The DLP printer was also equipped with an ultrafast curing module (CL1800, Carima, Republic of Korea), a 405 nm UV light source of 1800 W, and an air cooling system. Following printing, the scaffolds were photocrosslinked using 365 nm UV irradiation for 1–2 min. The printed scaffolds were stored in DMEM for pH adjustment in vitro cell culture.

**Chemical Characterization: Rheological analysis:** The rheological analysis was carried out using an ARES-G2 rheometer (TA Instruments, New Castle, Delaware, USA) with a 6 mm parallel plate at RT. The hydrogels were characterized by flow sweeps. GelMA hydrogel without CNC was considered the control group.

**Swelling test:** To measure the swelling ratio, the 3D-printed samples ( $10 \times 10 \times 5$  mm) were freeze-dried, and the dry weight of the samples was recorded ( $W_{\text{dry}}$ ). Next, the samples were immersed in 1 mL  $1 \times$  PBS at  $37^{\circ}\text{C}$  to reach equilibrium swelling. Finally, the scaffolds were blotted, and the swollen weight of each sample was recorded ( $W_{\text{wet}}$ ) at different time intervals (0, 2, 8, 10, and 12 h). The swelling ratio was calculated according to the equation

$$\text{Swelling ratio (\%)} = \frac{W_{\text{wet}} - W_{\text{dry}}}{W_{\text{dry}}} \times 100 \quad (1)$$

**Morphological analysis:** The morphology of the printed scaffolds was analyzed by an SEM (UR-SEM, Hitachi-S4800, CA, USA) with an acceleration voltage of  $15.0 \text{ kV cm}^{-1}$ . All the images were taken at 500 nm, 5, and 200  $\mu\text{m}$  resolution and compared with the control. The Perkin Elmer FTIR analyzer (Frontier, Perkin Elmer, UK) was used to evaluate the functional groups present in the sample in a transmitted mode in the wavenumber range of  $4000\text{--}1000 \text{ cm}^{-1}$  with a resolution of  $4 \text{ cm}^{-1}$ .  $^1\text{H}$  NMR spectra were collected using an NMR spectrometer (JEOL CO, Ltd., Tokyo, Japan). The structural properties of the GelMA and CelMA hydrogels were investigated using AFM and SAXS analysis. The interaction between CNC and GelMA was further evaluated using the XPS and conductive titration analysis under ambient condition.

**Mechanical test:** Compression test was carried out using MCT-1150 (A&D, Japan) instrument at a test speed of  $10 \text{ mm min}^{-1}$ . Young's modulus of the 3D-printed CelMA scaffold was calculated by determining the slope of the linear region of the stress–strain curve.

**In Vitro Study: Cell culture:** The hBMSCs were received from the Korean Cell Line Bank (KCLB, Seoul, Republic of Korea) and cultured using DMEM supplemented with 10% FBS and 1% antibiotics containing penicillin ( $10\,000 \text{ units mL}^{-1}$ ), streptomycin ( $10\,000 \mu\text{g mL}^{-1}$ ), and amphotericin B ( $25 \mu\text{g mL}^{-1}$ ) at  $37^{\circ}\text{C}$  in a humidified atmosphere of 5%  $\text{CO}_2$  (Steri-Cycle 370 Incubator; Thermo Fisher Scientific, USA). The hBMSCs were seeded on the printed GelMA and GelMA-CNC scaffolds and cultured under static conditions for 24 h. Following the cell attachment, one set of hBMSC laden GelMA and GelMA-CNC scaffolds were used for

pulsatile pressure stimulation for 20 min under an average pressure stimulation of  $10.37 \pm 2.94 \text{ kPa}$ . Cells without pressure stimulation were taken as control. Passage 5 cells were used in this study. For osteogenic induction, the cells were cultured in an osteogenic induction media containing DMEM supplemented with  $50 \mu\text{g mL}^{-1}$  L-ascorbic acid,  $10 \times 10^{-3} \text{ M}$   $\beta$ -glycerophosphate, and  $100 \times 10^{-9} \text{ M}$  dexamethasone.

**Cell viability assay:** The hBMSCs ( $1 \times 10^4$  cells/100  $\mu\text{L}$  media) were seeded into a 96-well plate and incubated with GelMA-CNC scaffolds containing 2% CNC at  $37^{\circ}\text{C}$  with 5%  $\text{CO}_2$  for the chosen periods (1, 3, and 5 days). The hBMSCs cultured with GelMA scaffold were considered as control. The cell viability was analyzed using WST-8 assay. After the desired cultured period, 10  $\mu\text{L}$  of the WST-8 dye was added and incubated for 2 h. The produced formazan was quantitated by measuring the absorbance at 450 nm (625 nm as a reference value). All the experiments were accomplished in triplicate, and data are presented as mean ODs  $\pm$  standard deviations. Statistical significance was considered at  $*p < 0.05$ .

**Live–dead assay:** The hBMSCs ( $4 \times 10^4$  cells/100  $\mu\text{L}$  media) were seeded on GelMA and GelMA-CNC scaffolds in a 6-well plate at  $37^{\circ}\text{C}$  with 5%  $\text{CO}_2$  under static and pressure stimulation. The survivability of the PPS-treated cells was analyzed using live–dead fluorescence imaging after 3 days of incubation. The cells grown under static culture were taken as control. For the live–dead assay, the cells were washed with  $1 \times$  PBS, followed by treatment with 1  $\mu\text{L}$  of Acridine orange and ethidium bromide dye solution at a ratio of 1:1. The images were captured immediately on appropriate filter channels using Leica Microsystems Suite X software (Leica Microsystems, Germany) of the inverted fluorescence microscope (DMI8 Series, Leica Microsystems, Germany).

**Assessment of ROS:** The  $\text{H}_2\text{O}_2$ -induced oxidative stress in hBMSCs was assessed in the presence of PPS by observing the formation of free radical species using dichlorodihydrofluorescein diacetate (DCF-DA) staining, qRT-PCR analysis, and GSH activity. Briefly, cells were cultured at a density of  $2 \times 10^4$ . Next, the cells and the positive control were incubated with  $200 \times 10^{-6} \text{ M}$   $\text{H}_2\text{O}_2$  for 20 min at  $37^{\circ}\text{C}$  in the  $\text{CO}_2$  incubator. Cells without an  $\text{H}_2\text{O}_2$  treatment were taken as the negative control. Upon PPS, cells were incubated with  $20 \times 10^{-6} \text{ M}$  DCF-DA for 30 min. After that, the cells were washed with PBS, and the nucleus was counterstained with DAPI for 30 s. The DCF-DA fluorescence intensity was checked using a fluorescence microscope (ex/em = 485/538). The respective intensities of the DCF-DA were measured using ImageJ software (ImageJ v1.8, NIH Lab., Bethesda, MD, USA, https://imagej.nih.gov/) for the quantitative analysis of the formation of intracellular ROS. For qRT-PCR analysis,  $4 \times 10^4$  cells were seeded onto the surface of the 3D-printed hydrogels (GelMA) and cultured until confluency. Next, the cells were stimulated using PPS (20 min) and the total RNA was harvested using TRIzol method according to the manufacturer's instruction. After that, the cDNA was synthesized from 2  $\mu\text{g}$  of RNA using reverse transcriptase and SYBR Green Master mix. The mRNA expression was quantified with a Bio-Rad Real-Time PCR (CFX96TM Maestro Real-Time System, Bio-Rad, USA) to identify the expression of the ROS sensitive or scavenging genes (*SOD2*, *NOX4*, *CAT*, *TXNR1*, and *Gpx*). The specified primers sequences are listed in Table S1 in the Supporting Information. For GSH activity, the total protein was harvested using radioimmunoprecipitation assay buffer. After that, 0.2 mL of protein lysate was mixed with 1 mL of  $0.5 \times 10^{-3} \text{ M}$  5,5-dithio-bis-(2-nitrobenzoic acid) (DTNB) and incubated for 5 min at RT. Next, the total GSH activity was quantified spectrophotometrically at 405 nm. Data reported as mean  $\pm$  SD of triplicate ( $n = 3$ ) experiments.

**Actin Morphology:** The arrangement of F-actin and paxillin was studied through fluorescence imaging to visualize the effect of PPS on the cell cytoskeleton. After 3 days of culture, the hBMSCs ( $2 \times 10^4$  cells/100  $\mu\text{L}$  media) were cultured on GelMA and CelMA scaffolds under static and PPS. The cells were washed with PBS and fixed with 3.7% paraformaldehyde (PFA) for 15 min at RT, followed by the addition of 0.1% Triton X-100 to permeabilize the cells for 10 min at RT. The cells were rinsed twice with PBS buffer and blocked for 1 h with 1% bovine serum albumin (BSA). After this, the cells were incubated for 1 h with 200  $\mu\text{L}$  mouse anti-human paxillin (ex/em = 488/520) at a dilution of 1:300 in BSA. The permeabilized cells were rinsed with PBS and then incubated for 30 min with a 200  $\mu\text{L}$  Alexa Fluor (AF) 488 F-actin probe (ex/em = 488/518) to visualize the F-actin.

The nuclear staining was done by adding 20  $\mu\text{L}$  of 1  $\text{mg mL}^{-1}$  DAPI solution for 2 min in the dark. The stained cells were rinsed and covered with a mounting medium and a glass coverslip. The fluorescence images were taken with a microscope at a magnification of 40x. The region of interest intensity of the images was quantified using ImageJ software (ImageJ v1.8, NIH Lab., USA, [www.imagej.nih.gov](http://www.imagej.nih.gov)).

**Mineralization Study:** The effect of PPS on the mineralization of hBMSCs was evaluated by the ARS procedure after 7 days of stimulation. The cultured cells on the scaffold were rinsed with PBS. The cells were fixed and permeabilized with 1 mL of 70% absolute ice-cold ethanol for 15 min at RT. The permeabilized cells were stained with 500  $\mu\text{L}$  of  $40 \times 10^{-3}$  M ARS (pH 4.2) stain for 10 min, followed by washing with deionized water to remove the excess stain. The mineralization was documented using the optical microscope.

**RNA Isolation, qRT-PCR Analysis, and Transcriptome Analysis:** The expression of the osteogenic-marker genes in pressure-treated and control cells was evaluated by the qRT-PCR technique. Briefly, the cells ( $4 \times 10^4$  cells/100  $\mu\text{L}$  media) were cultured under the experimental conditions in the osteogenic induction media for 7 days, followed by the extraction of RNA by TRIzol reagent (Thermo Fisher Scientific, USA), according to the manufacturer's instructions. The purity and concentration of the extracted RNA were evaluated by a spectrophotometer. The cDNA was synthesized from 2  $\mu\text{g}$  of RNA using reverse transcriptase and SYBR Green Master mix. The mRNA expression was quantified with a Bio-Rad Real-Time PCR (CFX96TM Maestro Real-Time System, Bio-Rad, USA). The reaction condition included 43 cycles of denaturation for 15 s at 95  $^{\circ}\text{C}$  and 1 min amplification at 60  $^{\circ}\text{C}$ . All the experiments were performed in triplicate and normalized to the housekeeping gene GAPDH. The relative mRNA expression from hBMSCs in the presence of PPS and control was compared in a histogram. All the samples were prepared in triplicate during the experiments. The specific gene primers used for qRT-PCR analysis were reported previously.<sup>[46]</sup>

**Immunocytochemical Staining:** The expression of the osteogenic marker proteins was studied through an immunocytochemical staining procedure. The hBMSCs ( $4 \times 10^4$  cells/100  $\mu\text{L}$  media) were cultured for 7 days under static and pulsatile pressure culture conditions. The cells were stained by washing with PBS, followed by fixing with 3.7% PFA for 15 min at RT. Next, the cells were permeabilized by adding 0.1% Triton X-100 for 10 min at RT. After that, the cells were rinsed twice with PBS, blocked by 1% BSA, and incubated with 250  $\mu\text{L}$  of mouse monoclonal antibodies against Runx2 and ALP. The nucleus was counterstained with 20  $\mu\text{L}$  of 1  $\text{mg mL}^{-1}$  DAPI solution for 2 min in the dark. The fluorescence images were taken with a microscope at a magnification of 40x.

**C5 Cytokine Antibody Array:** Following the manufacturer's instructions, the human C5 cytokine array (RayBiotech, Inc.) was used to identify the secreted cytokine profile in the mechanically stimulated cells. The densitometry data were obtained using Image J software.

**Transcriptome Analysis:** The transcriptome analysis was conducted to evaluate the DEGs in various experimental groups. The total RNA was harvested after 7 days of osteogenic differentiation by RNAzol (Sigma-Aldrich, USA) reagent and used to prepare the standard RNA library. The QuantSeq 3' mRNA-Seq was performed using a next-generation RNA sequencer (Nova-Seq 6000, PE100 bp, CA, USA) using the reference genome hg19 and genome database UCSC for humans. The raw data was processed using the ExDEGA graphic software (ebiogen, Republic of Korea) and normalized to log<sub>2</sub> (average of normalized data in each group), and statistical analysis was carried out using Student's *t*-test. The genes (up/downregulated) with a fold change of  $\geq 2.0$  and a *p* value  $< 0.05$  were considered statistically significant. STRING software (<https://string-db.org/>) was used to evaluate the possible interaction and co-expressed gene and protein networks.

**Statistical Analysis:** Statistical analysis for all in vitro data analysis was performed using OriginPro 9.0 software. Statistical significance between the control and treatment groups was determined using one-way analysis of variance. All the data were presented as mean  $\pm$  SDs. Differences were considered significant at  $*p < 0.05$ ,  $**p < 0.01$ ,  $***p < 0.001$ . The RNA sequencing data were normalized through TMM and CPM methods using the edgeR package. The obtained *p*-values were corrected for mul-

tiples comparisons using Benjamin and false discovery rate using DAVID software (<https://david.ncifcrf.gov/tools.jsp>).

## Supporting Information

Supporting Information is available from the Wiley Online Library or from the author.

## Acknowledgements

This work was supported by the Starting Growth Technological R&D program (S2840309, Development of a novel bioreactor system with stimuli for stem cell cultures) funded by the Small and Medium Business Administration (SMBA), and was also funded by 'the Basic Science Research Program' through the 'National Research Foundation of Korea' funded by the Ministry of Education (NRF-2018R1A6A1A03025582, NRF-2019R1D1A3A03103828, and NRF-2022R11A3063302).

## Conflict of Interest

The authors declare no conflict of interest.

## Data Availability Statement

The data that support the findings of this study are available from the corresponding author upon reasonable request.

## Keywords

osteogenesis, pulsatile pressure stimulation, soft hydrogels, stem cells, transcriptome

Received: August 25, 2022

Revised: December 20, 2022

Published online:

- [1] a) W. Wang, K. W. Yeung, *Bioact. Mater.* **2017**, *2*, 224; b) J. C. Reichert, A. Cipitria, D. R. Epari, S. Saifzadeh, P. Krishnakanth, A. Berner, M. A. Woodruff, H. Schell, M. Mehta, M. A. Schuetz, *Sci. Transl. Med.* **2012**, *4*, 141ra93.
- [2] a) A. J. Engler, S. Sen, H. L. Sweeney, D. E. Discher, *Cell* **2006**, *126*, 677; b) M. Guvendiren, J. A. Burdick, *Nat. Commun.* **2012**, *3*, 792; c) Y. Zhang, Z. Li, J. Guan, Y. Mao, P. Zhou, *AIP Adv.* **2021**, *11*, 010701; d) E. H. Chung, M. Gilbert, A. S. Virdi, K. Sena, D. R. Sumner, K. E. Healy, *J. Biomed. Mater. Res., Part A* **2006**, *79*, 815; e) A.-M. Poblath, S. Checa, H. Razi, A. Petersen, J. C. Weaver, K. Schmidt-Bleek, M. Windolf, A. Á. Tatai, C. P. Roth, K.-D. Schaser, *Sci. Transl. Med.* **2018**, *10*, eaam8828.
- [3] a) S. Chen, H. Wang, V. L. Mainardi, G. Talò, A. McCarthy, J. V. John, M. J. Teusink, L. Hong, J. Xie, *Sci. Adv.* **2021**, *7*, eabg3089; b) Y. Zhou, X. Xin, L. Wang, B. Wang, L. Chen, O. Liu, D. W. Rowe, M. Xu, *npj Regener. Med.* **2021**, *6*, 34; c) L. Cheng, T. Lin, A. T. Khalaf, Y. Zhang, H. He, L. Yang, S. Yan, J. Zhu, Z. Shi, *Sci. Rep.* **2021**, *11*, 4283; d) M. Govoni, L. Vivarelli, A. Mazzotta, C. Stagni, A. Maso, D. Dallari, *Materials* **2021**, *14*, 3290.
- [4] a) D. E. Discher, P. Janmey, Y.-I. Wang, *Science* **2005**, *310*, 1139; b) F. Chowdhury, S. Na, D. Li, Y.-C. Poh, T. S. Tanaka, F. Wang, N. Wang, *Nat. Mater.* **2010**, *9*, 82; c) T. H. Kim, D. B. An, S. H. Oh, M. K. Kang, H. H. Song, J. H. Lee, *Biomaterials* **2015**, *40*, 51; d) P. Han, J. E. Frith, G. A. Gomez, A. S. Yap, G. M. O'Neill, J. J. Cooper-White, *ACS Nano* **2019**, *13*, 11129.

- [5] A. K. Jha, W. M. Jackson, K. E. Healy, *PLoS One* **2014**, *9*, e98640.
- [6] L. E. Jansen, N. P. Birch, J. D. Schiffman, A. J. Crosby, S. R. Peyton, *J. Mech. Behav. Biomed. Mater.* **2015**, *50*, 299.
- [7] Q. Wei, J. Young, A. Holle, J. Li, K. Bieback, G. Inman, J. P. Spatz, E. A. Cavalcanti-Adam, *ACS Biomater. Sci. Eng.* **2020**, *6*, 4687.
- [8] L. E. Jansen, H. Kim, C. L. Hall, T. P. McCarthy, M. J. Lee, S. R. Peyton, *Biomaterials* **2022**, *280*, 121270.
- [9] M. Zhang, Q. Sun, Y. Liu, Z. Chu, L. Yu, Y. Hou, H. Kang, Q. Wei, W. Zhao, J. P. Spatz, *Biomaterials* **2021**, *268*, 120543.
- [10] J. Li, W. Wang, M. Li, P. Song, H. Lei, X. Gui, C. Zhou, L. Liu, *Front. Bioeng. Biotechnol.* **2021**, *9*, 770049.
- [11] a) J. Liu, Z. Zhao, J. Li, L. Zou, C. Shuler, Y. Zou, X. Huang, M. Li, J. Wang, *J. Cell. Biochem.* **2009**, *107*, 224; b) J. Liu, Z. Zhao, L. Zou, J. Li, F. Wang, X. Li, J. Zhang, Y. Liu, S. Chen, M. Zhi, *Ann. Biomed. Eng.* **2009**, *37*, 794; c) D. H. Kim, S.-H. Kim, S.-J. Heo, J. W. Shin, S. W. Lee, S. A. Park, J.-W. Shin, *J. Biosci. Bioeng.* **2009**, *108*, 63; d) R. Hess, T. Douglas, K. A. Myers, B. Rentsch, C. Rentsch, H. Worch, N. G. Shrive, D. A. Hart, D. Scharnweber, *J. Biomech. Eng.* **2010**, *132*, 021001; e) E. G. Meyer, C. T. Buckley, A. Steward, D. Kelly, *J. Mech. Behav. Biomed. Mater.* **2011**, *4*, 1257.
- [12] Z. Luo, B. Seedhom, *Proc. Inst. Mech. Eng., Part H* **2007**, *221*, 499.
- [13] E. Stavenschi, M. A. Corrigan, G. P. Johnson, M. Riffault, D. A. Hoey, *Stem Cell Res. Ther.* **2018**, *9*, 276.
- [14] E. H. Nguyen, W. T. Daly, N. N. T. Le, M. Farnoodian, D. G. Belair, M. P. Schwartz, C. S. Lebakken, G. E. Ananiev, M. A. Saghiri, T. B. Knudsen, *Nat. Biomed. Eng.* **2017**, *1*, 0096.
- [15] a) E. Kaemmerer, F. P. Melchels, B. M. Holzapfel, T. Meckel, D. W. Huttmacher, D. Loessner, *Acta Biomater.* **2014**, *10*, 2551; b) R.-Z. Lin, Y.-C. Chen, R. Moreno-Luna, A. Khademhosseini, J. M. Melero-Martin, *Biomaterials* **2013**, *34*, 6785; c) M. Zhu, Y. Wang, G. Ferracci, J. Zheng, N.-J. Cho, B. H. Lee, *Sci. Rep.* **2019**, *9*, 6863; d) M. A. Sakr, K. Sakthivel, T. Hossain, S. R. Shin, S. Siddiqua, J. Kim, K. Kim, *J. Biomed. Mater. Res., Part A* **2022**, *110*, 708.
- [16] a) W. Zhu, H. Cui, B. Boualam, F. Masood, E. Flynn, R. D. Rao, Z.-Y. Zhang, L. G. Zhang, *Nanotechnology* **2018**, *29*, 185101; b) I. Pelplanova, K. Kruppa, T. Scheper, A. Lavrentieva, *Bioengineering* **2018**, *5*, 55; c) M. Zhou, B. H. Lee, Y. J. Tan, L. P. Tan, *Biofabrication* **2019**, *11*, 025011.
- [17] a) H. Shin, B. D. Olsen, A. Khademhosseini, *Biomaterials* **2012**, *33*, 3143; b) E. Hoch, C. Schuh, T. Hirth, G. E. Tovar, K. Borchers, *J. Mater. Sci.: Mater. Med.* **2012**, *23*, 2607; c) W. T. Brinkman, K. Nagapudi, B. S. Thomas, E. L. Chaikof, *Biomacromolecules* **2003**, *4*, 890.
- [18] J. W. Nichol, S. T. Koshy, H. Bae, C. M. Hwang, S. Yamanlar, A. Khademhosseini, *Biomaterials* **2010**, *31*, 5536.
- [19] S. M. Saraiva, S. P. Miguel, M. P. Ribeiro, P. Coutinho, I. J. Correia, *RSC Adv.* **2015**, *5*, 63478.
- [20] Y. Wu, A. Wenger, H. Golzar, X. S. Tang, *Sci. Rep.* **2020**, *10*, 20648.
- [21] L. Wei, J. Huang, Y. Yan, J. Cui, Y. Zhao, F. Bai, J. Liu, X. Wu, X. Zhang, M. Du, *ACS Appl. Polym. Mater.* **2022**, *4*, 4876.
- [22] P. Chansoria, S. Asif, K. Polkoff, J. Chung, J. A. Piedrahita, R. A. Shirwaiker, *ACS Biomater. Sci. Eng.* **2021**, *7*, 5175.
- [23] K. Ganguly, H. Jin, S. D. Dutta, D. K. Patel, T. V. Patil, K.-T. Lim, *Carbohydr. Polym.* **2022**, *287*, 119321.
- [24] A. H. Milani, L. A. Fielding, P. Greensmith, B. R. Saunders, D. J. Adlam, A. J. Freemont, J. A. Hoyland, N. W. Hodson, M. A. Elsayy, A. F. Miller, *Chem. Mater.* **2017**, *29*, 3100.
- [25] S. Xiao, T. Zhao, J. Wang, C. Wang, J. Du, L. Ying, J. Lin, C. Zhang, W. Hu, L. Wang, *Stem Cell Rev. Rep.* **2019**, *15*, 664.
- [26] S. J. Mlakar, J. Osredkar, J. Prezelj, J. Marc, *Menopause* **2012**, *19*, 368.
- [27] a) H. Byun, G. N. Jang, J. Lee, M.-H. Hong, H. Shin, H. Shin, *Biofabrication* **2021**, *13*, 034101; b) A. I. Rupérez, A. Gil, C. M. Aguilera, *Int. J. Mol. Sci.* **2014**, *15*, 3118.
- [28] D. S. Amarasekara, H. Yun, S. Kim, N. Lee, H. Kim, J. Rho, *Immune Netw.* **2018**, *18*, e8.
- [29] Y. Yang, T. Xu, H.-P. Bei, L. Zhang, C.-Y. Tang, M. Zhang, C. Xu, L. Bian, K. W.-K. Yeung, J. Y. H. Fuh, *Proc. Natl. Acad. Sci. U. S. A.* **2022**, *119*, e2206684119.
- [30] a) G. Xi, C. Wai, V. DeMambro, C. J. Rosen, D. R. Clemmons, *J. Bone Miner. Res.* **2014**, *29*, 2427; b) Z. Zhang, X. Zhang, D. Zhao, B. Liu, B. Wang, W. Yu, J. Li, X. Yu, F. Cao, G. Zheng, *Mol. Med. Rep.* **2019**, *19*, 3505; c) S. Um, J.-H. Lee, B.-M. Seo, *Int. J. Oral. Sci.* **2018**, *10*, 29; d) H. Y. Yim, C. Park, Y. D. Lee, K.-I. Arimoto, R. Jeon, S. H. Baek, D.-E. Zhang, H.-H. Kim, K. I. Kim, *J. Immunol.* **2016**, *196*, 3887; e) X. Feng, S. Shen, P. Cao, L. Zhu, Y. Zhang, K. Zheng, G. Feng, D. Zhang, *Cytotechnology* **2016**, *68*, 2699; f) D. Lee, K.-J. Shin, D. W. Kim, K. Yoon, Y.-J. Choi, B. N. R. Lee, J.-Y. Cho, *Cell Death Dis.* **2018**, *9*, 495.
- [31] C. Shen, C. Yang, S. Xu, H. Zhao, *Cell Biosci.* **2019**, *9*, 17.
- [32] A. Meixner, F. Karreth, L. Kenner, J. M. Penninger, E. F. Wagner, *Cell Death Differ.* **2010**, *17*, 1409.
- [33] S. S. Ranade, R. Syeda, A. Patapoutian, *Neuron* **2015**, *87*, 1162.
- [34] D. De Felice, A. Alaimo, *Cancers* **2020**, *12*, 1780.
- [35] L. Qin, T. He, S. Chen, D. Yang, W. Yi, H. Cao, G. Xiao, *Bone Res.* **2021**, *9*, 44.
- [36] Z. Qiu, A. E. Dubin, J. Mathur, B. Tu, K. Reddy, L. J. Miraglia, J. Reinhardt, A. P. Orth, A. Patapoutian, *Cell* **2014**, *157*, 447.
- [37] N. C. Henney, B. Li, C. Elford, P. Reviriego, A. K. Campbell, K. T. Wann, B. A. Evans, *Am. J. Physiol.: Cell Physiol.* **2009**, *297*, C1397.
- [38] M. Dejaeger, A. M. Böhm, N. Dirckx, J. Devriese, E. Nefyodova, R. Cardoen, R. St-Arnaud, J. Tournoy, F. P. Luyten, C. Maes, *J. Bone Miner. Res.* **2017**, *32*, 2087.
- [39] a) X. Cao, E. Ban, B. M. Baker, Y. Lin, J. A. Burdick, C. S. Chen, V. B. Shenoy, *Proc. Natl. Acad. Sci. U. S. A.* **2017**, *114*, E4549; b) S. Kwon, W. Yang, D. Moon, K. S. Kim, *Cancer Cell Int.* **2020**, *20*, 217.
- [40] C. Zhou, L. H. Lyu, H. K. Miao, T. Bahr, Q. Y. Zhang, T. Liang, H. B. Zhou, G. R. Chen, Y. Bai, *Mol. Carcinog.* **2020**, *59*, 545.
- [41] a) G. L. Galea, M. R. Zein, S. Allen, P. Francis-West, *Dev. Dyn.* **2021**, *250*, 414; b) J. Schuelke, N. Meyers, S. Reitmaier, S. Klose, A. Ignatius, L. Claes, *PLoS One* **2018**, *13*, e0195466.
- [42] Y. Sun, B. Wan, R. Wang, B. Zhang, P. Luo, D. Wang, J.-J. Nie, D. Chen, X. Wu, *Front. Cell Dev. Biol.* **2022**, *10*, 808303.
- [43] F. M. Shaikh, T. P. O'Brien, A. Callanan, E. G. Kavanagh, P. E. Burke, P. A. Grace, T. M. McGloughlin, *Artif. Organs* **2010**, *34*, 153.
- [44] W. Xu, B. Z. Molino, F. Cheng, P. J. Molino, Z. Yue, D. Su, X. Wang, S. Willför, C. Xu, G. G. Wallace, *ACS Appl. Mater. Interfaces* **2019**, *11*, 8838.
- [45] L. MacQueen, Y. Sun, C. A. Simmons, *J. R. Soc., Interface* **2013**, *10*, 20130179.
- [46] a) K. Ganguly, S. D. Dutta, M.-S. Jeong, D. K. Patel, S.-J. Cho, K.-T. Lim, *PLoS One* **2021**, *16*, e0249291; b) S. D. Dutta, J. Hexiu, D. K. Patel, K. Ganguly, K.-T. Lim, *Int. J. Biol. Macromol.* **2021**, *167*, 644.